



The effect of surface wettability on flow boiling characteristics within microchannels

Konstantinos Vontas*, Manolia Andredaki, Anastasios Georgoulas, Nicolas Miché, Marco Marengo

Advanced Engineering Centre, School of Computing, Engineering and Mathematics, University of Brighton, Lewes Road, BN2 4GJ, Brighton, East Sussex, UK

ARTICLE INFO

Article history:

Received 25 November 2020

Revised 31 January 2021

Accepted 17 February 2021

Keywords:

flow boiling

microchannels

multiphase flow

VOF

conjugate heat transfer

surface wettability

ABSTRACT

The process of flow boiling within micro-passages plays a very important role in many industrial applications. However, there is still a lack of understanding of the effect of an important controlling parameter: surface wettability. In this paper, an advanced numerical investigation on the effect of wettability characteristics on single and multiple bubble growth during saturated flow boiling conditions within a microchannel is performed. The 3D numerical simulations are conducted with the open-source Computational Fluid Dynamics (CFD) toolbox OpenFOAM, utilising a custom user-enhanced Volume Of Fluid (VOF) solver. The proposed solver enhancements involve an appropriate treatment for spurious velocities damping, an improved dynamic contact angle treatment, as well as the implementation of a phase-change model in the fluid domain also accounting for Conjugate Heat Transfer (CHT) with the solid domain. In total, three sets of simulations of hydrophilic and hydrophobic surfaces with constant heat and mass flux were performed. In the first set, a single bubble seed was patched close to the inlet of the microchannel and the Heat Transfer Coefficient (HTC) along the channel interface was measured until the nose of the bubble reaches the outlet. The bubble growth and transport process within the channel were analysed, with a minor effect of the wettability characteristics on the HTC observed. In the second set of simulations, multiple recurring nucleation events at the same position were simulated; observing that in such more realistic cases the effect of wettability in the HTC was more profound. Finally, simulations with multiple nucleation sites and recurring nucleation events were conducted to analyse cases closer to reality. These results show indeed that surface wettability plays a significant role on the HTC, with the hydrophilic and hydrophobic cases performing approximately 43.9% and 17.8% higher respectively, compared to the single-phase reference simulations. Additionally, it is found that the dominant heat transfer mechanisms for the hydrophilic and hydrophobic surface are liquid film evaporation and contact line evaporation, respectively, and that for the proposed simulation parameters liquid film evaporation can be considered as a more efficient heat transfer mechanism compared to contact line evaporation.

© 2021 Elsevier Ltd. All rights reserved.

1. Introduction

Significant advancements in the electronic industry have led to high demands of devices/products which generate substantial amounts of heat during their operation. These devices have many components that are attached to electronic circuit boards, generating heat when operating. Therefore, an important aspect that needs to be taken into consideration, when designing such devices, is their thermal management. Their performance can be significantly affected by the attained temperature levels, and overheating should be avoided, since it can reduce their lifetime drastically

or even cause an untimely failure [1]. Among the aforementioned devices, the microprocessor chips (microchips) constitute major sources of heat generation. Microchips, due to their small size and high-performance, have a very high-power density per unit area with localized hot spots which lead to high operating temperatures, and hence, there is a risk of overheating. In more detail, investigations have reported that the average heat flux in computer chips is predicted to reach 2–4.5 MW/m² by 2026 [2], while the next generation of computer chips is expected to produce localized heat fluxes over 10 MW/m² [3]. The highest values of heat flux at the chip level can be found in Insulated Gate Bipolar Transistors (IGBTs), where heat fluxes can reach values as high as 6.5–50 MW/m² [4]. Conventional cooling methods, such as air convection through fans or pumped liquid cooling, cannot cope with such high rates of heat-dissipation. Hence, new more efficient

* Corresponding author.

E-mail address: k.vontas@brighton.ac.uk (K. Vontas).

cooling methods have been proposed and developed in the past decades [5–7]. Flow boiling heat transfer within microchannels has been recognized experimentally as one of the most efficient thermal management solutions for such high-power density electronic components, dissipating heat fluxes in the order of MW/m² [8–10]. However, the lack of accurate design correlations, as well as the limitation of understanding of several underpinned principles and mechanisms, have hampered the transition of this cooling method from the laboratory to commercial applications. Karayiannis and Mahmood [2], reported that there are still open fundamental research aspects and issues in flow boiling in microchannels (e.g. flow patterns and heat transfer mechanisms, flow instabilities and encountered pressure drops). The effect of the solid surface characteristics on the underpinned bubble dynamics and heat transfer constitutes another important parameter where further research is needed. Particularly, parameters such as the solid surface manufacturing method, the application of surface coatings to enhance heat transfer and the solid surface material properties might all significantly affect the underpinned phenomena and mechanisms [11–13]. Surface wettability is considered a critical parameter in micro-scale phenomena as well, especially in confined two-phase flows within micro-passages, where the surface tension force becomes dominant as the size decreases [14]. Therefore, many investigations under different experimental conditions have been focused on surface wettability effects of two-phase flows within microchannels [15–18]. Nevertheless, as reported by Kandlikar [19], despite the fact that wettability effects are quite important in flow boiling within microchannels, there is a lack of available experimental reports having considered flow boiling within micro-scale channels in the literature. According to Kandlikar & Willmar [20], the main reason for this could be the difficulties of fabrication. Some older and more recent experimental investigations on wettability effects of flow boiling in microchannels are summarised in the following paragraphs.

Flow boiling experiments which studied the effects of wettability in multiple small channels were first studied by Rioboo et al. [21]. In this work deionized Milli-Q water is used. Hydrophilic ($\theta_a/\theta_r = 107.3^\circ/80.3^\circ$) and hydrophobic ($\theta_a/\theta_r = 94.8^\circ/55.5^\circ$) surfaces heated on the bottom side (500W) have been used, whereas the liquid mean velocities tested were 0.0309 and 0.0386 m/s. Overall channel dimensions were L, W, H: 18, 0.1 and 0.6 mm. It was found that phase change is due to the local density of nanobubbles and this depends on the surface hydrophobicity. Additionally, chemical heterogeneities and wettability contrast are found to be strongly affected on global heat flux on the solid surface. Biphilic surfaces of microchannels have also been studied in the recent years, since they can take advantage of both hydrophilic and hydrophobic surfaces and thus achieve high boiling heat transfer performance. Wang et al. [22] experimentally studied the wettability effects of a chemically-patterned surface and compared the results with homogeneous hydrophilic microchannel with hydraulic diameter of 311.76 μm and heat flux values between 25.6 kW/m² to 786.1 kW/m². It was found that the HTC increased up to 22% for the patterned surface in comparison to the hydrophilic microchannel and when the mass flux increases, HTC is accordingly enhanced. An enhanced HTC and CHF of heterogeneous surfaces is also reported by Kim et al. [23] who tested flow boiling performance of water on a hydrophilic (57°) rectangular channel with hydraulic diameter 7.5mm coated with SiO₂, having hydrophobic (120°) stripes with different widths and directions coated with Teflon. Particularly, it was observed that higher HTC and CHF was generated for narrow patterns, compared to the wide patterns. The influence of heterogeneous wetting surfaces was explored also numerically by Kim et al. [24] who tested a rectangular channel of a hydrophilic (30°) surface combined with hydrophobic (110°) patterns (crosswise, parallel and dotted). The working fluid

was water, and the hydraulic diameter was 0.95mm, while constant heat flux of 350 kW/m² is applied, whereas the mass flux values ranged between 100–800 kg/m²s. Their model included a nucleation site density correlation. They found that nucleation site density was higher for the case of the dotted patterns at high mass fluxes resulting to better heat transfer performance. However, very wide or narrow hydrophobic areas result to reduced heat transfer performance. Since however, the present investigation is focused on homogeneous wettability surfaces the following paragraphs review works on microchannels with homogeneous wettability.

Phan et al. [25] conducted an experimental investigation of flow boiling of water in rectangular microchannels with the applied heat flux varied from 30 kW/m² to 80 kW/m², with different vapour qualities. In total, three hydrophilic plus one hydrophobic surface with equilibrium contact angles of 26°, 49°, 63° and 104° respectively were used. From the experiments, it was shown that different flow patterns such as bubbly flow, slug flow, and semi-annular flow resulted in a significant variation on the overall heat transfer. Additionally, it was also observed that when the contact angle increases, the superheat needed for onset of nucleate boiling decreases. They concluded that a low superheat for onset of nucleate boiling, in combination with good control of bubbles emission frequency, is an important factor in improving the heat transfer performance of flow boiling within microchannels.

Concerning the evaluation of the flow boiling hydraulic and thermal performance in microchannels, Liu et al. [26] performed experiments of three identical geometries of 105, 1000 and 30000 μm^3 , with different wettability characteristics. The three examined surfaces included a super-hydrophilic surface after growth of nanowire arrays with a contact angle of almost 0°, a plain silicon wafer hydrophilic surface machined through plasma etching with a contact angle of 36° and a hydrophobic surface coated by a thin film of low surface energy material with a contact angle of 103°. Different boiling flow patterns on surfaces with different wettabilities were observed, leading to a large difference in the resulting temperature oscillations and hence in the HTC. In detail, for the super-hydrophilic case a generation of a high number of bubble nuclei was observed, possibly due to the associated surface cavities formed between the nano-spaced rings on the nanowire fabricated surface. For the hydrophilic case, a more cyclic flow process occurred, that was mainly associated with the nucleation, growth and coalescence of bubbles. Finally, for the hydrophobic surface, boiling was found to begin at a slightly higher heat flux compared to the hydrophilic surfaces, resulting a severe superheat of the liquid phase prior to bubble nucleation, leading to fast growth of nucleated bubbles after boiling incipience, was observed.

More recently, Li et al. [27] conducted an experimental study of saturated water flow boiling in a bare silicon wafer hydrophilic surface, which was later altered to a super-hydrophilic one, after being deposited by nanoscale silicon dioxide particles, with deposition thickness of 100 nm through the Plasma Enhanced Chemical Vapour Deposition (PECVD) process. The corresponding contact angles were measured to be 65° and less than 5°, respectively. The applied heat flux values ranged between 40 to 200 kW/m², while the mass fluxes spanned from 120 to 360 kg/m²s. It was reported that in the annular flow regime, the local HTC decreased until approaching a minimum value and later increased towards the exit along the flow direction. At low mass flux and high vapour quality, a delay of partial dryout occurrence on the super-hydrophilic surface was observed. The averaged HTC of the hydrophilic surface decreased with increments of heat or mass flux, indicating that in the bared wall hydrophilic surface dryout patches and high wall temperature are more easily formed in comparison to the super-hydrophilic surface. Another study on subcooled boiling in microchannels using the same set-up as in [27], but with the possibility of varying the channel orientation, was conducted by Li et al.

[28]. The applied heat fluxes were ranged from 40 to 250 kW/m² and the mass fluxes from 200 to 500 kg/m²s. It was shown that due to the enhancement of convective heat transfer caused by bubble disturbance near the exit and the suppression of nucleate boiling caused by high subcooling close to the entrance, the HTC increased along the flow direction. An earlier occurrence of the Critical Heat Flux value (CHF) was observed for the cases of vertical downflows. It was also shown that at low mass flux, the super-hydrophilic surface delays CHF without an increased pressure drop penalty, when it is in a vertical orientation either in an upflow or downflow configuration. By changing the orientation to horizontal, the super-hydrophilic surface showed a higher heat transfer coefficient by 10% with a corresponding 37% increase in the pressure drop for the bottom-heated flow, while for the top-heated flow, the HTC decreased by 16% and the pressure drop increased by 15%, compared to the hydrophilic surface. It was concluded that the effect of surface wettability is more significant in the horizontal orientation.

Choi et al. [29] conducted experiments of flow boiling of water in rectangular hydrophilic and hydrophobic microchannels, in order to investigate the effect of wettability. It was reported that the HTC of the hydrophobic microchannel was higher than the hydrophilic microchannel, mostly due to the associated nucleation site density and the resulting flow instabilities. However, the pressure drop in the hydrophobic surface was higher than that of the hydrophilic case, due to the unstable motion of bubbles and the formation of liquid films.

Numerical investigations in wettability effects of flow boiling in microchannels are even more limited in the literature, mainly due to the complex physics involved with such micro-scale two-phase flows and also due to the fact that the available contact angle treatments in commercial as well as opensource CFD codes are failing to accurately capture the dynamic nature of the apparent contact angles during bubble growth. Gong & Cheng [30] developed a 2D model where the Lattice Boltzmann method (LBM) was utilised. The effects of contact angle, inlet velocity, and heater size on the resulting flow patterns, under constant heat flux conditions, were studied. Their model could also provide information about nucleation time and temperature using empirical correlation. The results showed that the static contact angle does not influence the bubble departure size. Nevertheless, nucleation time and nucleation temperature appeared to decrease when contact angle is increased. Examining the resulting Nusselt numbers, an increase was observed with the increase of the Re number or with an increase in the superheat degree. Conversely, a corresponding decrease in the resulting Nusselt numbers with an increase in the imposed contact angle was found. Finally, along the centreline in the superheated liquid from the inlet to the outlet, the pressure was shown to drop almost linearly, except from the exit region of the flow where unphysically large pressure jumps and drops in liquid-vapour interface regions were observed, which were attributed to the equation of state for real gases adopted in the model. The same authors have also utilised their LBM model for studying the effects of surface wettability on pool boiling heat transfer on the bubble departure diameter, nucleation site density and onset of nucleate boiling, for hydrophilic, hydrophobic and mixed wettability surfaces [31,32]. Wettability effects on pool boiling was also numerically studied by Hsu et al. [33] who developed boiling curves for various hydrophilic and hydrophobic contact angles.

Wettability and inertia effects on heat transfer during flow boiling in microchannels were numerically investigated by Kim & Lee [34]. A constant heat flux of 350 kW/m² was applied at the bottom surface of the utilised rectangular channel with dimensions (L, W, H: 30, 0.2 and 0.5 mm), while the mass flux value varied between 20 and 500 kg/m²s. A hydrophilic and a hydrophobic surface with contact angles of 30° and 110°, respectively, were

utilised. The computational mesh consisted of 1.536 M cells with 12.5µm cell size. In their numerical model the fluid interface is tracked by the volume of fluid approach, while the same phase change model as proposed by Hardt and Wondra [35] was used. Their model included also a nucleation site density utilising empirical correlation. For the prediction of the contact angle, a dynamic contact angle model based on Tanner's Law was used. Their results were compared with experimental data available in literature. From their results it was observed that wettability did not influence the flow patterns when cases with the same mass flux were compared. By increasing the mass flux different flow patterns could be seen (annular flow at 20 kg/m²s, churn flow at 50 kg/m²s, slug flow at 100 kg/m²s, confined bubble flow at 200 kg/m²s and bubbly flow for mass fluxes above 300 kg/m²s). With regards to the temperature of the channel, at low mass flux, a higher temperature could be seen in the hydrophobic surface due to the presence of a thin liquid film which is covering the interface between the solid and the vapour and is working as lubricant. Under low mass fluxes (20-100 kg/m²s), hydrophilic channel had higher CHF compared to the hydrophobic. This trend was reversed for high heat fluxes (200-500 kg/m²s). Finally, the numerical model overestimated HTC approximately 10% compared to the experimental results, concluding that the model can be adequately used for boiling simulations in microchannels.

A 3D Conjugate numerical study of flow boiling in diverging mini and microchannels with different inlet and outlet width (between 0.2 and 0.8mm) in order to investigate the bubble pattern and heat transfer characteristics of flow boiling, has been carried out by Alugoju et al [36]. The simulations were performed by using the volume of fluid method of ANSYS-FLUENT® 18.0, coupled with a phase change and a surface tension force model. A uniform heat flux condition varying between 500 and 2000 kW/m² is applied at the bottom surface of the channel, with the rest of the walls to be considered adiabatic, while the mass flux ranges between 240 and 710 kg/m²s. A hydrophilic and a hydrophobic surface were utilised with contact angles of 65° and 140°, respectively, while water was used as the working fluid. Empirical correlations proposed by Bertsch et al. [37] which account for convective heat transfer and nucleate boiling terms were included in the model. They reported that different bubble patterns between the two surfaces were observed. Particularly, for the hydrophilic case the bubble separation rate from the wall is less, thereby creating localized hotspots, while for the hydrophobic surface the generated bubbles are detached from the wall surface and flow along with the fluid stream. Other observations included that when the hydraulic diameter is increased, smaller elongated bubbles are observed. In smaller channels and at low flow rate localized flow reversal could be seen. Finally, for some cases when the mass flux increases higher values of localized heat transfer could be seen in channels with lower hydraulic diameter, and as the diameter is increased, the values are reduced, due to the different nucleation time and bubble pattern.

As it can be seen from all these works, there is a considerable influence of wettability on flow boiling characteristics within micro-passages. However, so far most of the experimental investigations related to surface characteristics and/or wettability effects are focusing on heat transfer enhancement's underpinned physical mechanisms, whereas how heat transfer coefficient is enhanced is still not completely understood. Additionally, in the experimental investigations, different solid materials are used in order to alter the surface wettability characteristics, or the channel surfaces are treated accordingly through the application of coatings [38] that alter the structure, properties and the chemical composition of the surfaces. This might lead to the alteration of other factors, apart from the solid/liquid/vapour contact angle, that can additionally affect the flow boiling characteristics, such as the nucleation site

density and the solid surface thermal response. Therefore, the exact effect of wettability cannot be isolated and directly identified and quantified, utilising experimental measurements. On the other hand, the numerical investigations available in literature can isolate the effect of wettability by altering only the contact angle, however in most of the cases they use dynamic contact angle models which have been found to be less accurate [39]. Additionally, the examined ranges of contact angles in the literature are not wide enough to adequately capture the effects of hydrophilicity or hydrophobicity, taking also into account the effect of contact angle hysteresis. The present numerical investigation aims for the first time in the literature to isolate, identify and quantify in detail the effect of wettability on the average local and global heat transfer characteristics for cases of saturated flow boiling within smooth rectangular micro-passages by “virtually” altering the advancing and receding contact angles for the case of single and multiple recurring, bubble nucleation events, that grow within a microchannel. Advancing and receding contact angle values, corresponding to super-hydrophilic, hydrophilic as well as hydrophobic single rectangular channels, are simulated for this purpose, for different values of applied heat flux and mass flux.

2. Numerical Simulation Framework

The numerical simulations of the present paper are conducted with the open-source toolbox OpenFOAM, utilising a user-enhanced Volume of Fluid (VOF) solver. The proposed solver enhancements involve a treatment for spurious velocities dampening (a well-known defect of VOF methods), an improved dynamic contact angle treatment to accurately account for wettability effects as well as the implementation of a phase-change model in the fluid domain, accounting for conjugate heat-transfer with a solid domain. It should be mentioned that liquid and vapour phases are both treated as incompressible Newtonian fluids. The proposed solver has been extensively validated in the past against various cases of adiabatic and diabatic bubble and droplet dynamics in comparison with available analytical solutions as well as experimental measurements by the authors' research team. A detailed description of the numerical framework can be found in [40–43,49].

3. Application of the numerical model

3.1. Computational geometry and boundary conditions

The computational mesh has been generated by discretising the computational domain in two parts. The solid domain and the fluid domain. A uniform, structured computational mesh, consisting of hexahedral elements is utilised. The physical dimensions of the fluid domain (length, height and width) are $L_f = 2.40$ mm, $H_f = 0.30$ mm, $W_f = 0.15$ mm ($D_h = 0.2$ mm) and the solid domain dimensions are $L_s = 2.40$ mm, $H_s = 0.09$ mm, $W_s = 0.15$ mm, respectively. The generated computational geometry, the mesh and the applied boundary conditions are illustrated in Fig. 1. These dimensions have been selected in order to represent typical rectangular microchannel geometries from the literature [44].

With regards to the boundary conditions, apart from the inlet and outlet in the fluid domain and the bottom side of the solid domain, where a constant heat flux is applied, all the rest surfaces are considered to be adiabatic walls. At the solid walls of the fluid domain, a standard no-slip velocity boundary condition is used with a fixed flux pressure boundary condition for the pressure values. Additionally, a value of the dynamic contact angle is imposed for the liquid volume fraction field by assigning the maximum advancing and minimum receding contact angle values from sessile drop measurements, that are then used for the calculation

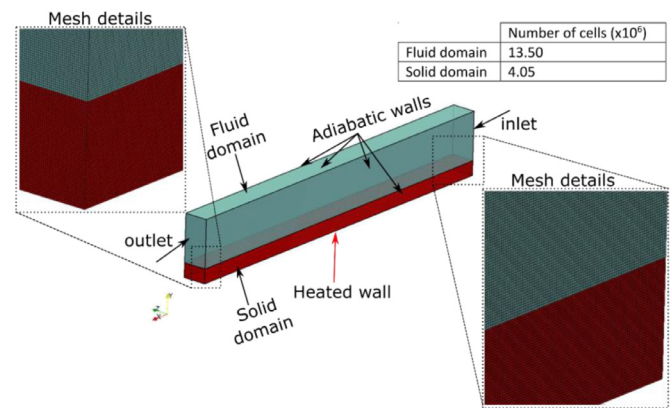


Fig. 1. Computational domain, boundary conditions and mesh details.

of the theoretical dynamic contact angle values during the computations, using a model originally suggested by Kistler. For the side-walls of the fluid and solid domains, a zero gradient boundary condition is used for the temperature field. At the outlet, a fixed-value pressure boundary condition and a zero-gradient boundary condition for the volume fraction were used, while for the velocity values a special (combined) type of boundary condition is used that applies a zero-gradient when the fluid mixture exits the computational domain and a fixed value condition to the tangential velocity component, in cases that the fluid mixture enters the domain. Finally, a zero gradient boundary condition for the temperature field was also prescribed at the outlet boundary. For the inlet, a constant uniform velocity value was imposed as well as a fixed flux pressure condition. The volume fraction value was assigned as unity, as saturated liquid only enters from the inlet during the calculations. Hence, the temperature of the liquid at the inlet was also fixed at the saturation temperature. As mentioned earlier both the temperature values as well as the heat fluxes are coupled at the conjugate heat transfer interface (between the solid and fluid domains) for each calculation time step through an inner iteration process.

3.2. Numerical simulation set-up and process

As shown in Fig. 1, the considered configuration for the present parametric numerical investigation consists of a single microchannel with a uniform heat flux q'' applied at its bottom solid wall. Therefore, the generated 3D computational domain consists of a solid domain (representing the bottom solid wall of the channel) that is in contact with the fluid domain that corresponds to the considered micro-passages. All the simulations are performed in two stages. During the first stage, a specified heat flux is applied to the bottom surface of the solid domain and a single-phase liquid flow is considered initially with saturated liquid, flowing with a specified mass flow rate. This is run up to a point that a steady state condition is reached and both the hydrodynamic and thermal boundary layers have been developed, as shown in Fig. 2a. The velocity of the liquid U_l is constant and uniform through the inlet boundary and the flow is laminar. The first stage is conducted for all simulations presented in this paper. At the second stage (Fig. 2b) a small vapour nucleus (bubble seed), represented as a half-sphere with a radius of 20 μ m, is patched onto the conjugate heat transfer boundary (interface between the fluid and solid domains) at a distance of 200 μ m from the channel inlet, at saturation temperature. Since the initial bubble seed is patched within the previously developed thermal boundary layer, where the temperature is higher than the saturation temperature, boiling occurs at the meniscus (solid/liquid/vapour triple line) as well as at the

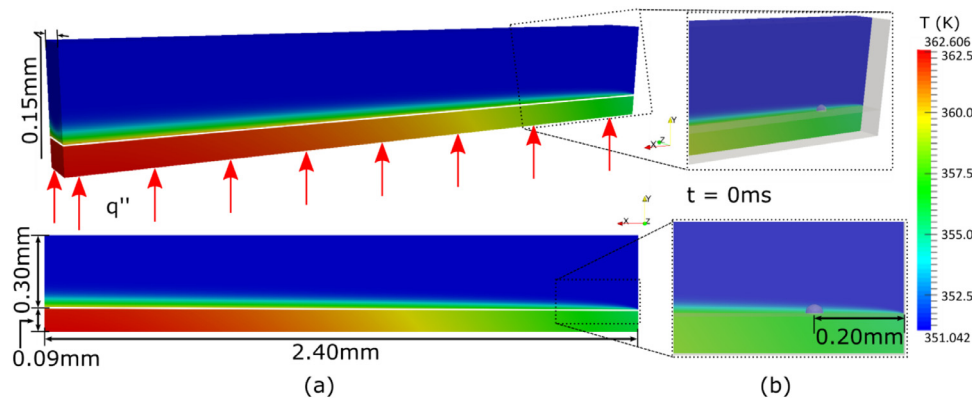


Fig. 2. (a) Developed thermal boundary layer at the end of the first stage of simulations (single-phase), (b) patched bubble seed position at the beginning of the second phase of simulation (referred as initial time $t = 0$ ms), for $q'' = 20 \text{ kW/m}^2$ and $G = 150 \text{ kg/m}^2\text{s}$.

Table 1

Ethanol properties at saturation temperature that were used in the simulations.

$T/(\text{K})$	$P_{\text{sat}}/(\text{Pa})$	$\rho_l/(\text{kg/m}^3)$	$\rho_v/(\text{kg/m}^3)$	$\nu_l/(\text{m}^2/\text{s})$	$\nu_v/(\text{m}^2/\text{s})$	$\lambda_l/(\text{W/mK})$	$\lambda_v/(\text{W/mK})$
351.05	100,000	736.78	1.63	6.01×10^{-8}	6.37×10^{-8}	0.153	0.02

Table 2

Steel properties that were used for the simulations.

$\rho_s/(\text{kg/m}^3)$	$c_{p(s)}/(\text{J/KgK})$	$k_s/(\text{W/mK})$
7840	500	16.2

Table 3

Considered wettability characteristics (all these cases are considered for $q'' = 20, 50, 100 \text{ kW/m}^2$ and $G = 74, 150, 295 \text{ kg/m}^2\text{s}$).

Case	Surface	$\theta_a/(^{\circ})$	$\theta_r/(^{\circ})$	CAH/ $(^{\circ})$
I	Hydrophilic / Low hysteresis	19	8	11
II	Hydrophilic / High hysteresis	49	0	49
III	Mild Hydrophilic / High hysteresis	72	40	32
IV	Mild Hydrophobic / Low hysteresis	105	95	10
V	Hydrophobic / High hysteresis	120	80	40
VI	Hydrophobic / Low hysteresis	120	115	5

parts of the liquid/vapour interface that is in contact with temperatures higher than the saturation temperature. At this point it should be mentioned that the present Authors' research Group is already working towards the development of physically derived, less empirical, nucleation models, utilising a novel Fluctuating Diffuse Interface approach [45] that will be in the future implemented in the presently used, custom VOF solver. However, for the purposes of the present paper the focus is on the effect of surface wettability on bubble dynamics and heat transfer characteristics in an already nucleated bubble or bubbles, and the implementation of a nucleation sub-model was outside the present scope. Furthermore, it should be mentioned that for all of the simulations conducted for the present investigation, the liquid and vapour phase properties are taken as these of ethanol liquid and vapour at the saturation equilibrium point for a pressure of $P_{\text{sat}} = 1 \text{ bar}$, which corresponds to a saturation temperature of $T_{\text{sat}} = 351.05 \text{ K}$ (REFPROP NIST software [46]). As for the solid domain stainless steel properties were used, for all cases. The exact values of the fluid and solid properties that were used in all simulations conducted for the purposes of the present paper are summarised in Tables 1 and 2, respectively. The advancing and receding contact angles for the base case of the present parametric analysis were taken as these of ethanol with a particular stainless-steel sample at an average roughness $R_a = 0.4 \mu\text{m}$, having values of $\theta_a = 19^{\circ}$ and $\theta_r = 8^{\circ}$, respectively. In order to investigate the isolated effect of wettability in the bubble growth characteristics as well as its effect in the local heat transfer, in the rest of the runs the values of θ_a and θ_r were varied, while all the rest fluid and solid properties and operating conditions were kept unaltered. The contact angle values that were selected for this purpose correspond to realistic contact angles for different combinations of ethanol as well as other working fluids (e.g. R-113, Glycerol and Water) with either uncoated or coated Stainless Steel samples of the same or different grades. For the exact fluid-solid combination contact angle values the reader

is referred to [47]. In order to observe the effects of wettability at different heat fluxes, the overall analysis for all of the selected contact angle values was performed for three different values of applied heat flux ($q'' = 20, 50, 100 \text{ kW/m}^2$) and three different values of mass flux ($G = 74, 150$ and $295 \text{ kg/m}^2\text{s}$, with the Re number being 33, 66 and 133, respectively). All these values, as well as the material of the solid domain, were selected due to the fact that they are often used in the literature on flow boiling experiments within micro-passages and have a broad range of applications [2].

In order to cover a wide range of CAs, the selected values represent cases of hydrophilic and hydrophobic surfaces with both small and high Contact Angle Hysteresis (CAH = $\theta_a - \theta_r$). The overall details, regarding the wettability characteristics considered for each of the applied heat and mass flux values in the numerical simulations, are summarised in Table 3. As it can be seen, a combination of six different advancing and receding contact angles have been chosen, and considering all heat fluxes and mass fluxes tested, 54 in total, 3D, transient, numerical simulations were performed. A High-Performance Computing (HPC) cluster was utilized for these runs. Each run required 100 computational cores. The duration of the computation for each of the nine single-phase simulations (one for each q'' value) was approximately 10 days, as seconds of real flow were required for a steady state condition to be reached. For the two-phase simulations the duration of the computation was only a couple of days since just a few milliseconds of real flow were required for the generated vapour bubble to reach the outlet of the channel. In total, more than 1 M core-hours were utilised for the overall runs that are presented in the present paper. A variable calculation time step was utilised for the two-phase runs with the

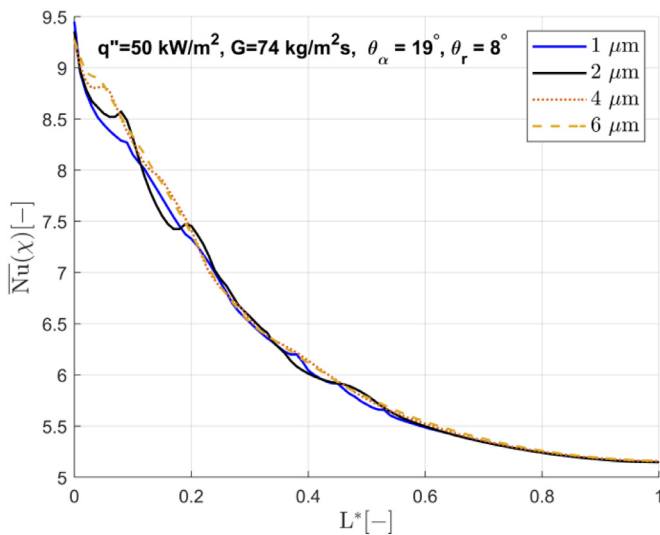


Fig. 3. Mesh independency study results for $q'' = 50 \text{ kW/m}^2$ and $G = 74 \text{ kg/m}^2\text{s}$. Hydrophilic surface $\theta_a = 19^\circ$, $\theta_r = 8^\circ$.

Courant number kept constant at 0.5. Hence the calculation time step was varied automatically ranging from 10^{-8} up to 10^{-6} s.

3.3. Mesh independency

A mesh independence study was carried out, in order to select the optimum cell size in the utilised, uniform, structured, computational mesh for the parametric numerical simulations. Four different structured meshes, consisting of hexahedral cells, were constructed for this purpose, with a uniform cell size of $6\mu\text{m}$, $4\mu\text{m}$, $2\mu\text{m}$ and $1\mu\text{m}$, respectively. The mesh independency study was performed for the case of $q'' = 50 \text{ kW/m}^2$, $G = 74 \text{ kg/m}^2\text{s}$ for a hydrophilic surface with $\theta_a = 19^\circ$ and $\theta_r = 8^\circ$. The material properties were those of ethanol liquid and vapour at the saturation equilibrium point of Table 1 for the fluid domain, while the stainless steel properties of Table 2 were used for the solid domain. The time-averaged local Nu number ($\overline{Nu}(x)$) over the non-dimensional length of the channel L^* ($L^* = L(x) / L_{\text{max}}$) predictions for all four computational meshes are compared in Fig. 3. The average relative errors of the $2\mu\text{m}$ case in comparison with the $1\mu\text{m}$ case is 0.28% and in comparison with the $4\mu\text{m}$ and $6\mu\text{m}$ cases, the average errors are 0.53% and 0.67%, respectively. The maximum local relative error of the $2\mu\text{m}$ case compared with the $1\mu\text{m}$, $4\mu\text{m}$ and $6\mu\text{m}$ cases is 1.63%, 2.72% and 3.36%, respectively. Hence, the selected mesh size of $2\mu\text{m}$ can be safely considered as the mesh independent solution. Furthermore, from previous investigations [40,41,43,48,49], where the same solver was utilised, it has been shown that a $2\mu\text{m}$ cell size is sufficient for capturing correct interface dynamics and evaporation rates. The selected mesh consists of a total number of 17.55M cells (4.05M cells in the solid and 13.50M cells in the fluid domain).

4. Numerical simulation results

4.1. Effect of wettability on micro-passages – Single nucleation site, single nucleation event

In this subsection the numerical results of flow boiling of a single nucleation event at a single nucleation site within a rectangular microchannel will be presented. As previously shown in Table 3, numerical simulations of three different heat flux values have been performed, each of them separately investigated with

three different mass flux values for six in total surfaces with different wettability characteristics (three hydrophilic and three hydrophobic surfaces). At this point, it is important to mention that in the present numerical model the nucleation event is not a result of the simulation but an imposed condition. In more detail, as also mentioned earlier, a single liquid-phase simulation is initially performed in order to develop the hydrodynamic and thermal boundary layers. Then a small bubble nucleus is artificially placed at the heated wall a finite distance from the microchannel inlet, that initiated the boiling process at that particular position, with a bubble that grows and either slides along the channel walls from the previously developed liquid-cross flow (being in contact at certain points with the channel walls) or detaches from the wall and continues its growth as an evaporating vapour slug, due to liquid film evaporation.

Indicative qualitative/macrosopic results of the spatial and temporal evolution of the generated vapour bubbles, for three different cases are shown in Figs. 4 and 5. In the isometric view snapshots, the coloured contours in the clip section that extends from one side of the channel up to its middle plane, reveal the developed temperature fields in both the fluid and solid regions of the computational domain. In the top view snapshots, the coloured contours also show the instantaneous temperature distribution in the CHT boundary, i.e. the interface between the fluid and solid domains. The transparent grey surface constitutes the liquid/vapour interface which is represented by the 0.5 volume fraction iso-surface.

Both Figs. 4 and 5 correspond to cases with low heat and mass flux. Fig. 4 compares hydrophilic cases and Fig. 5 hydrophobic cases. The spatial evolution of the liquid/vapour interface for three successive time instants is illustrated, in each case, through a 2D top view and a 3D isometric view. The first two time instants are common among the different wettability cases (0.9ms and 4.2ms), but the last time instant is chosen differently for each case, corresponding to the time that the leading edge of the bubble reaches the outlet of the channel. The macroscopic results of the remainder of the cases, for the rest of the tested mass fluxes and heat fluxes, due to space limitation, are only shown for the last time instant until the nose of the bubble touches the end of the microchannel, in Figs. 6, 7 and 8.

Focusing on Figs. 4 and 5, from a bubble dynamics point of view, a complete detachment of the bubble from the walls and the formation of a liquid film between the walls and the vapour bubble is observed for some of the cases, while, in some other cases, partial detachment or even no detachment with respect to the heated wall, as the bubble grows and slides towards the outlet, is observed. At this point, it should be mentioned that the imposed contact angles are applied for all walls of the channel and not only at the bottom heated wall.

In Figs. 4 and 5 the results for different wettability cases and for the low heat and mass fluxes ($q'' = 20 \text{ kW/m}^2$, $G = 74 \text{ kg/m}^2\text{s}$) are shown. When comparing the three hydrophilic surfaces to each other (Figs. 4a, 4b, 4c at instants $t=7.9\text{ms}$, $t=9.8\text{ms}$ and $t=13.1\text{ms}$, respectively) it is observed that for the low advancing contact angle case (Fig. 4a: $\theta_a = 19^\circ$, $\theta_r = 8^\circ$), a thin liquid film is formed between the bubble and the bottom heated wall as well as the top adiabatic wall of the considered microchannel in the frontal part of the bubble, while the remaining trailing part of the bubble is staying in direct contact with the bottom and top walls through a relatively large dry patch at the bottom wall and a smaller one at the top wall. It is also evident that the bubble is in contact with the side channel walls through almost its entire length. However, as the advancing contact angle is increasing the length of these dry patches decreases gradually (Fig. 4b: $\theta_a = 49^\circ$, $\theta_r = 0^\circ$) up to a point where no liquid film is present at all (Fig. 4c: $\theta_a = 70^\circ$, $\theta_r = 40^\circ$).

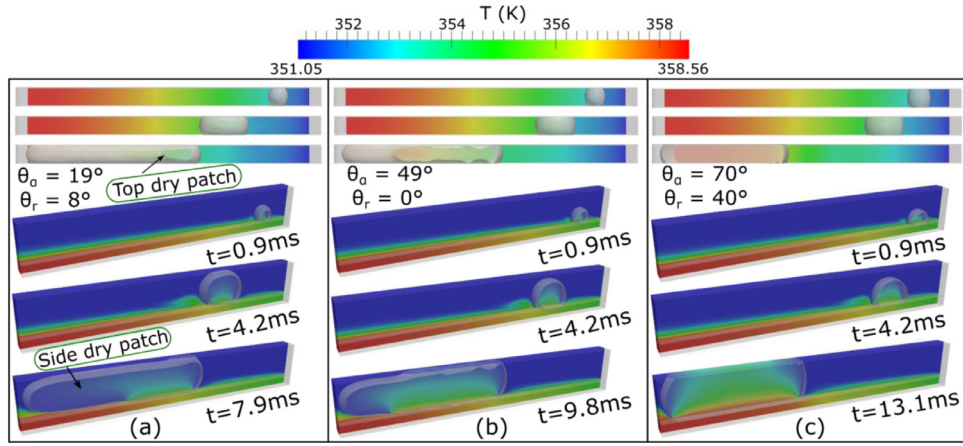


Fig. 4. Numerical flow visualisation results of hydrophilic cases, for $q'' = 20 \text{ kW/m}^2$ and $G = 74 \text{ kg/m}^2\text{s}$, (a) $\theta_a/\theta_r = 19^\circ/8^\circ$, (b) $\theta_a/\theta_r = 49^\circ/0^\circ$, (c) $\theta_a/\theta_r = 70^\circ/40^\circ$. In each case a 2D top view and a 3D isometric view of the phenomenon for two common time instants (0.9ms and 4.2ms) and a last time instant that corresponds to the time that the leading edge of the bubble reaches the outlet of the microchannel are shown.

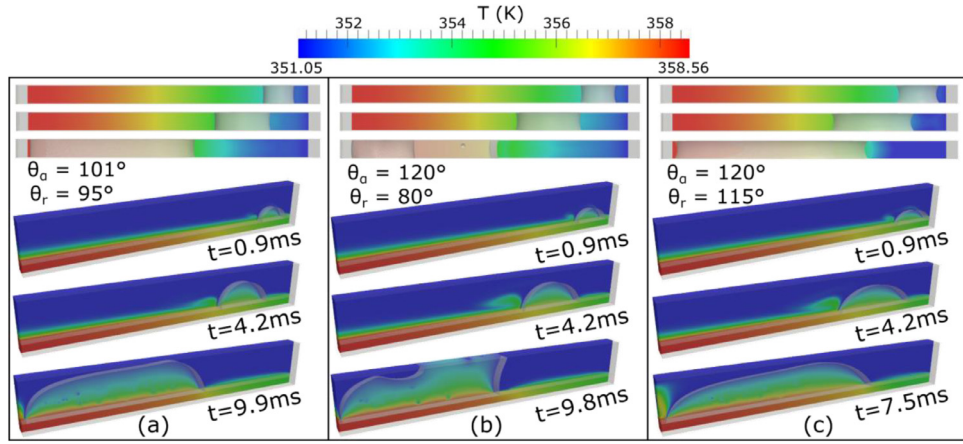


Fig. 5. Numerical flow visualisation results of hydrophobic cases for $q'' = 20 \text{ kW/m}^2$ and $G = 74 \text{ kg/m}^2\text{s}$, (a) $\theta_a/\theta_r = 101^\circ/95^\circ$, (b) $\theta_a/\theta_r = 120^\circ/80^\circ$, (c) $\theta_a/\theta_r = 120^\circ/115^\circ$. In each case a 2D top view and a 3D isometric view of the phenomenon for two common time instants (0.9 and 4.2ms) and a last time instant that corresponds to the time that the leading edge of the bubble reaches the outlet of the microchannel are shown.

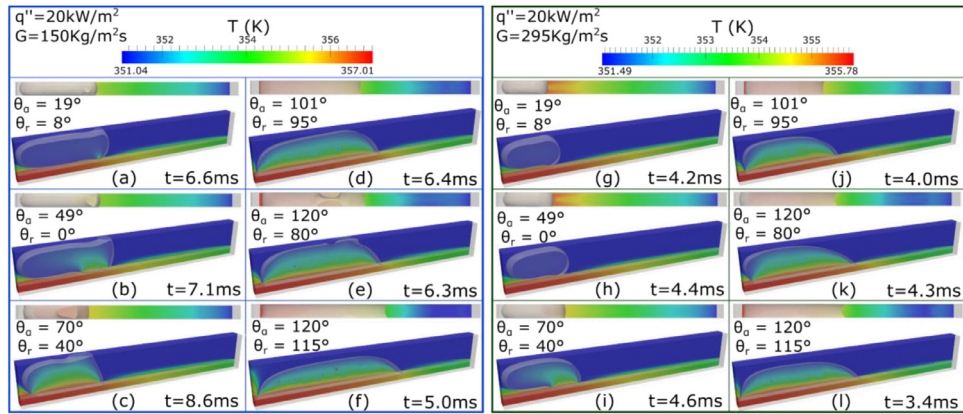


Fig. 6. Macroscopic view of the numerical simulation results, showing only the last time period before the bubble reaches the outlet of the microchannel for: $q'' = 20 \text{ kW/m}^2$ and $G = 150 \text{ kg/m}^2\text{s}$ (left), and $q'' = 20 \text{ kW/m}^2$ and $G = 295 \text{ kg/m}^2\text{s}$ (right).

As for the hydrophobic cases that are illustrated in Fig. 5, no presence of liquid film is observed as well. Therefore, it seems that there is a critical value of advancing contact angle ($\sim 70^\circ$) after which there is not any liquid film formation occurring. Furthermore, it is also evident that for the cases with small CAH ($\theta_a = 101^\circ$, $\theta_r = 95^\circ$ and $\theta_a = 120^\circ$, $\theta_r = 115^\circ$), the growing bubble remains in contact with the side and bottom wall of the channel

throughout its entire path within the microchannel without touching the top wall. However, for the higher CAH case ($\theta_a = 120^\circ$, $\theta_r = 80^\circ$), the generated vapour bubble comes also in contact with the top wall of the channel at a certain stage.

From all these macroscopic observations it can be concluded that, for relatively low heat and mass fluxes, the wettability has a quite significant effect in the resulting bubble growth char-

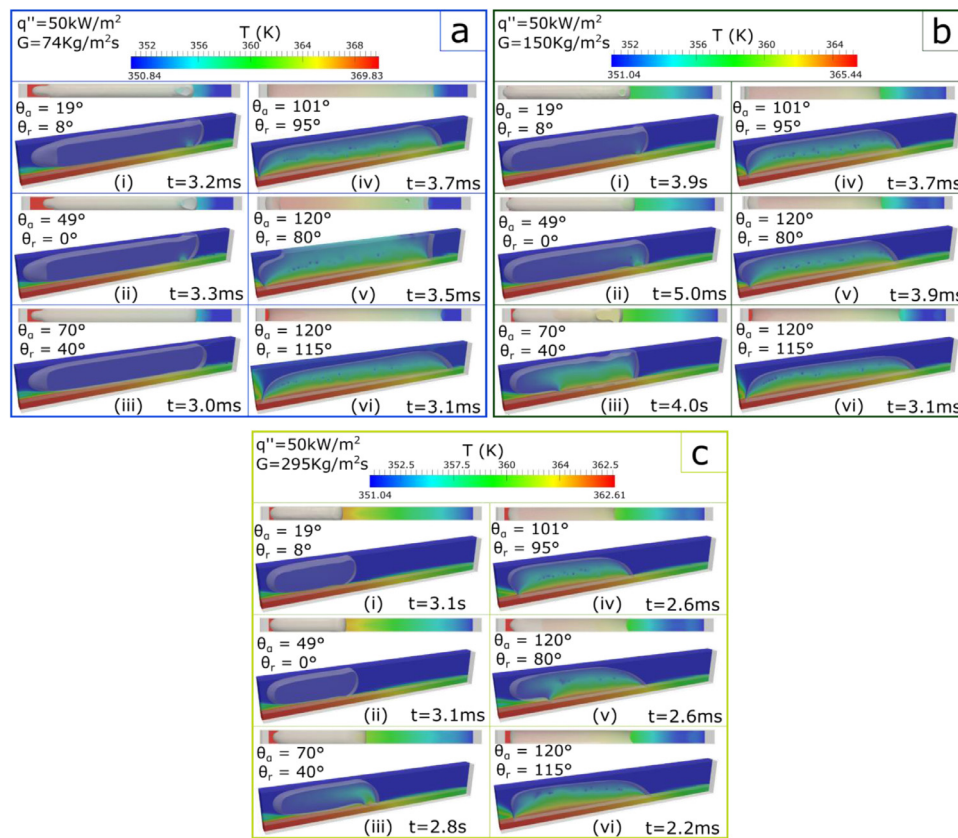


Fig. 7. Macroscopic view of the numerical simulation results for $q'' = 50 \text{ kW/m}^2$ at mass flux values 74, 150 and $295 \text{ kg/m}^2\text{s}$ from the top to the bottom box, respectively. In each box a 2D top view and a 3D isometric view for the last time period before the leading edge of the bubble touches the outlet of the microchannel for the six different wettability cases that are investigated, is shown.

acteristics as well as in the size and the shape of the bubble, resulting also in different contact line dynamics (i.e. triple liquid/vapour/solid line evolution behaviour). For all cases, due to the associated latent heat of evaporation, as the bubble grows and slides along the solid wall, the temperature of the solid is decreasing. Depending on the imposed contact angle values the bubble grows either due to evaporation at the triple line or to a combination of triple line evaporation and liquid film evaporation. The combination of the two mechanisms is more evident for relatively small contact angle values (i.e. more hydrophilic cases, Figs. 4a and 4b). The contribution of the liquid film evaporation to the overall evaporation rate is reduced as the hydrophilicity is reduced and it seems to be a threshold ($\theta_a \sim 70^\circ$), just after which the main evaporation mechanism is solely contact line evaporation (i.e. less hydrophilic and hydrophobic cases, Figs. 4c, 5a, 5b and 5c).

Fig. 6 illustrates only the last time period before the generated vapour bubble reaches the outlet of the channel, for two higher values of mass flux cases ($G = 150 \text{ kg/m}^2\text{s}$ and $G = 295 \text{ kg/m}^2\text{s}$), but for the same applied heat flux as in Figs. 4 and 5 ($q'' = 20 \text{ kW/m}^2$) for all of the considered wettabilities. As it can be seen, also for higher values of mass flux a similar trend is observed, with the development of liquid films for the low and medium hydrophilicity cases and direct contact of the vapour slug with the heated surface for the hydrophobic cases. It is also evident that as the mass flux increases and the heat flux remains constant, the contact areas of the generated vapour slugs with the heated wall are reducing in dimension. The overall volume of the vapour bubbles also seems to decrease with an increase of the mass flux. Finally, it is also evident that the increase of the mass flux tends to eliminate the previously observed trend of the generated vapour slug in the case of the high CAH hydropho-

bic surface to get in contact with the top wall of the channel (please see Figs. 6e and 6k).

Fig. 7, summarises the corresponding simulated flow visualisation results for the medium of the applied heat fluxes ($q'' = 50 \text{ kW/m}^2$), for all three of the considered mass flux values ($G = 74 \text{ kg/m}^2\text{s}$, $G = 150 \text{ kg/m}^2\text{s}$, $G = 295 \text{ kg/m}^2\text{s}$). In the hydrophilic cases, the leading edge of the bubble has developed a characteristic bullet-shape nose, which has a more rounded (less pointy) profile for the medium and high mass flux values, resulting in a slightly thinner liquid film compared to the simulation with the low mass flux. Very similar predictions can be seen between the two hydrophobic cases with low ($\theta_a = 101^\circ$, $\theta_r = 95^\circ$) and medium ($\theta_a = 120^\circ$, $\theta_r = 80^\circ$) advancing contact angles. In more detail, for $G = 74 \text{ kg/m}^2\text{s}$ and $G = 150 \text{ kg/m}^2\text{s}$ an almost complete detachment of the bubble is observed with respect to the heated wall, except for a small part in the trailing side of the bubble which remains in contact with the heated surface. However, a complete detachment and development of liquid film between the entire bottom side of the bubble and the heated wall can be seen when the mass flux is $295 \text{ kg/m}^2\text{s}$, meaning that the CAH difference between these two cases does not affect neither the bubble shape nor the bubble growth rate. Different behaviour is observed for the case with high hydrophilicity ($\theta_a = 70^\circ$, $\theta_r = 40^\circ$), where, for low mass flux, the bubble is entirely detached from the heated surface. However, for medium and high mass flux simulations, the high receding contact angle value, compared to the other two hydrophilic cases, has resulted to a partial contact of the bubble with the heated wall.

A contact area between the heated wall and the bubble is also observed, for the hydrophobic surface cases. Particularly, the cases with small CAH ($\theta_a = 101^\circ$, $\theta_r = 95^\circ$ and $\theta_a = 120^\circ$, $\theta_r = 115^\circ$)

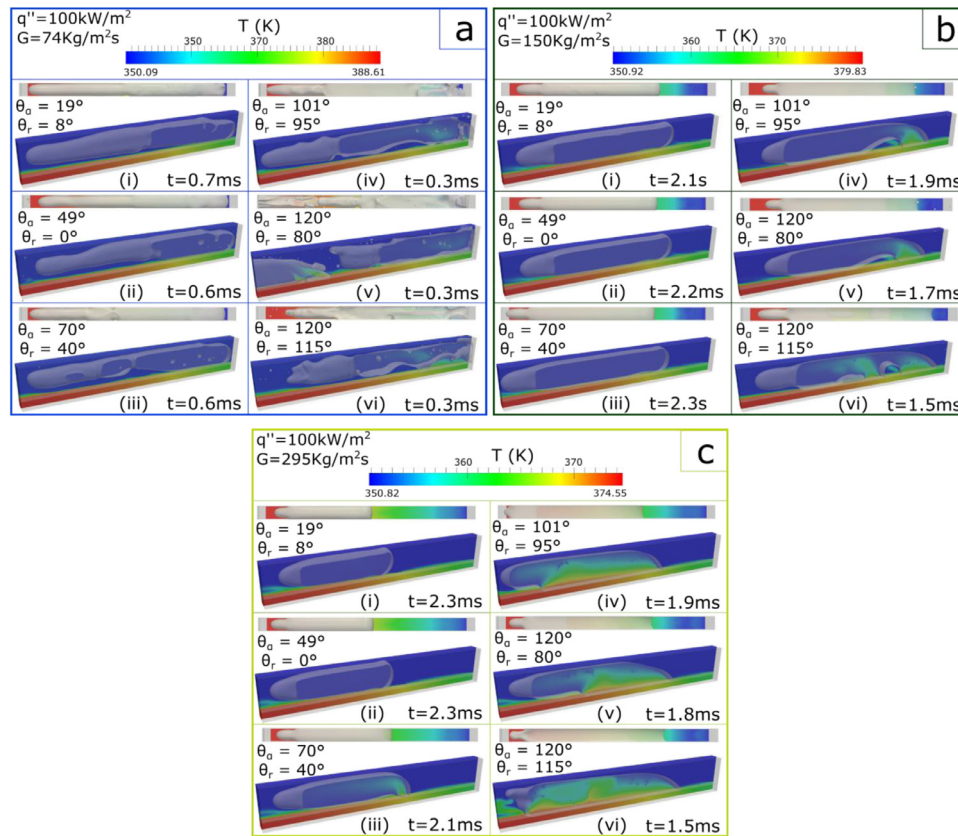


Fig. 8. Macroscopic view of the numerical simulation results for $q'' = 100 \text{ kW/m}^2$ at mass flux values 74, 150 and $295 \text{ kg/m}^2\text{s}$ from the top to the bottom box, respectively. In each box a 2D top view and a 3D isometric view for the last time period before the leading edge of the bubble touches the outlet of the microchannel for the six different wettability cases that are investigated, is shown.

maintain contact area with the heated wall throughout the entire bubble growth process, for all three mass flux cases. Conversely, when the mass flux is $295 \text{ Kg/m}^2\text{s}$ for the case with high CAH ($\theta_a = 120^\circ$, $\theta_r = 80^\circ$), about 70% of the bubble is still in contact with the heated wall, while the remainder 30% has similar shape as the one described previously for the hydrophilic cases, with presence of a thin liquid film between the bubble and the top and the bottom wall of the microchannel.

Finally, the corresponding qualitative results for the high heat flux value ($q'' = 100 \text{ kW/m}^2$) are illustrated in Fig. 8. For $G = 74 \text{ kg/m}^2\text{s}$ a different flow pattern is observed, compared to the cases with lower heat flux that have been discussed earlier. Particularly, for all the examined surfaces churn flow is observed. This can be attributed to the high wall superheat, which has resulted to a prompt growth of the nucleation bubble and unstable/ asymmetrical flow, for the first few time periods until the wall superheat is cooled down due to the heat transfer mechanisms. When the mass flux is increased to $G = 150 \text{ kg/m}^2\text{s}$ and $G = 295 \text{ kg/m}^2\text{s}$, a slug flow boiling regime is evident for both hydrophilic and hydrophobic cases. For the medium mass flux ($G = 150 \text{ kg/m}^2\text{s}$), a total detachment of the developed vapour bubble from the heated surface is observed for the hydrophilic cases. However, for the hydrophobic cases contact areas with the heated wall are observed mainly towards the trailing part of the generated bubbles. For the high mass flux simulations ($G = 295 \text{ kg/m}^2\text{s}$), the hydrophilic cases with low receding contact angle have detached from the heated wall, while the trailing part of the hydrophilic case with high receding contact angle maintains a contact with the heated surface.

From the overall flow visualisation results so far, the following conclusions can be drawn:

- 1) Slug flow boiling regime is observed in all cases, with the exception of the case with high heat flux and low mass flux, where a churn flow can be observed. In both flow regimes, the bubbles grow within a few milliseconds and fill almost the entire cross section of the microchannel.
- 2) Low heat flux or high mass flux (e.g. $q'' = 20 \text{ kW/m}^2$, $G = 295 \text{ kg/m}^2\text{s}$) is associated with smaller bubble sizes (less vapour volume). Conversely, high heat flux or low mass flux (e.g. $q'' = 100 \text{ kW/m}^2$, $G = 74 \text{ Kg/m}^2\text{s}$) is associated with higher bubble sizes (higher vapour volume).
- 3) The contact line areas with the heated wall is relatively small for the hydrophilic cases in comparison to the hydrophobic surfaces.
- 4) Apart from the heat and mass flux values, the wettability characteristics of the heated surface also determine the prevailing evaporation mechanism (liquid film versus contact line evaporation).
- 5) Liquid film evaporation is the main and sometimes the only heat transfer mechanism observed in hydrophilic surfaces, while in hydrophobic surfaces the dominant heat transfer mechanism is the contact line evaporation.
- 6) For all three of the examined heat fluxes the maximum values of the wall superheat decreases with the increase of the mass flux for both hydrophilic and hydrophobic surfaces.
- 7) When the wall superheat becomes significantly large, for the hydrophilic cases, the radius of the curvature of the nose decreases, resulting in a sharper nose, and hence, a thicker average liquid film (for the examined cases there is a threshold of $>19^\circ\text{C}$).
- 8) The receding contact angle value plays a significant role in the trailing part of the generated bubbles. In many cases, this value

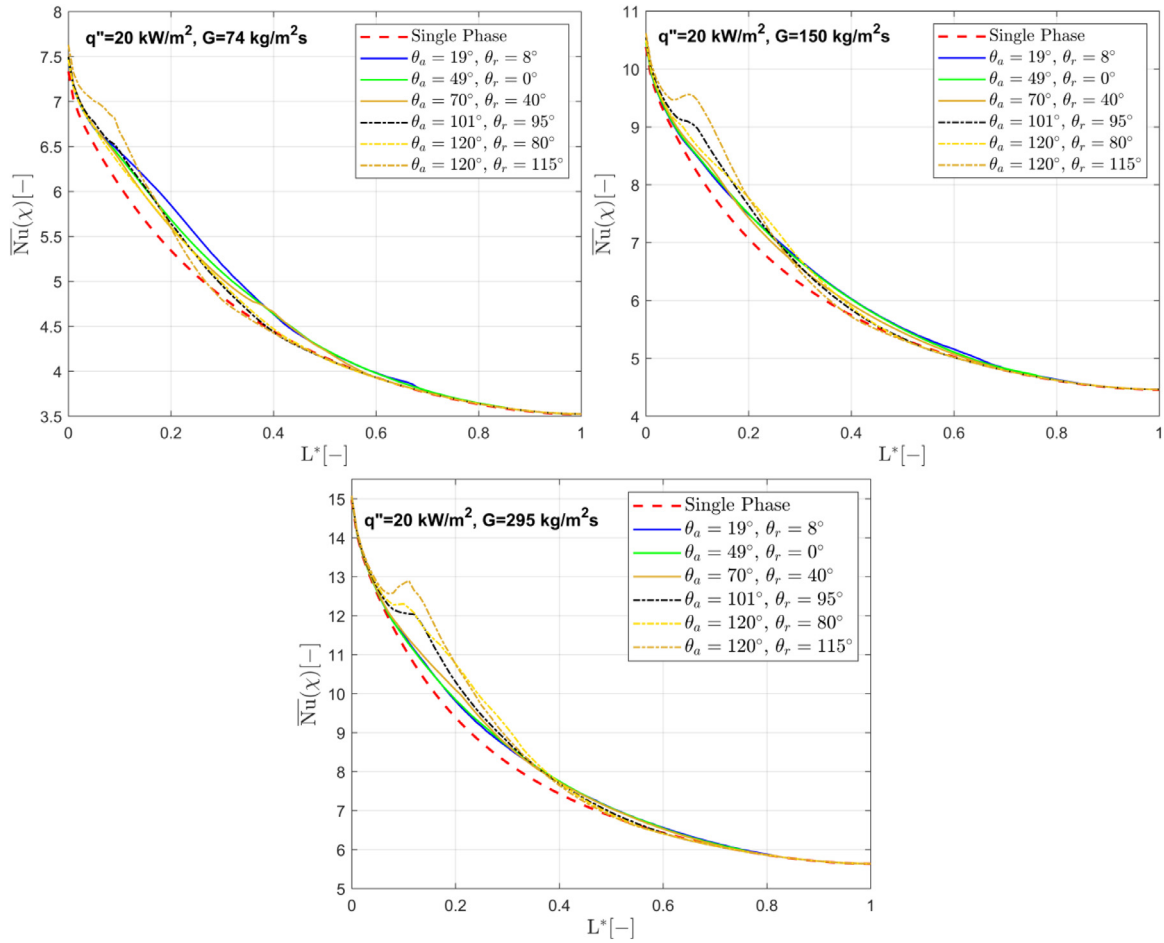


Fig. 9. Time-averaged local Nu along the conjugate heat transfer interface versus dimensionless Length for $q'' = 20 \text{ kW/m}^2$ and $G = 74, 150$ and $295 \text{ kg/m}^2\text{s}$.

Table 4

Percentage difference between the global Nu number of the two-phase stage of each run with the corresponding single-phase stage for $q'' = 20 \text{ kW/m}^2$ and $G = 74, 150$ and $295 \text{ kg/m}^2\text{s}$.

$\theta_a / (^\circ)$	$\theta_r / (^\circ)$	$G / (\text{kg/m}^2\text{s})$	$Nu_{glob} / (-)$	% Diff.	$G / (\text{kg/m}^2\text{s})$	$Nu_{glob} / (-)$	% Diff.	$G / (\text{kg/m}^2\text{s})$	$Nu_{glob} / (-)$	% Diff.
Single-phase		74	4.493	-	150	5.866	-	295	7.689	-
19	8		4.658	3.68		6.042	3.00		7.873	2.39
49	0		4.631	3.08		6.036	2.89		7.875	2.42
70	40		4.604	2.46		6.006	2.40		7.902	2.77
101	95		4.580	1.94		6.036	2.90		7.960	3.53
120	80		4.568	1.68		6.044	3.03		8.039	4.55
120	115		4.589	2.14		6.078	3.62		8.057	4.79

prevents a complete detachment of the bubble from the heated wall for the hydrophilic surfaces (especially at high mass flux) and sometimes for hydrophobic surfaces as well (at high heat flux).

In order to better identify and quantify the effect of wettability on flow boiling performance, quantitative results for the simulations, described above, are presented and discussed in the following paragraphs. Figs. 9, 10 and 11 report the dimensionless time-averaged local Nusselt numbers ($\overline{Nu}(x)$), over the dimensionless length of the channel L^* , for all of the examined advancing and receding contact angle combinations together with the single-phase stage of the proposed numerical runs that is used as reference, for each of the considered applied heat and mass fluxes, respectively. The percentage differences of the global Nusselt numbers (Nu_{glob}) for each advancing and receding contact angle combination with the corresponding Nu_{glob} of the single-phase stage of each numer-

ical run, are summarised in Tables 4, 5 and 6, for applied heat flux values of $q'' = 20, 50$ and 100 kW/m^2 , respectively.

In order to evaluate the local Nusselt number, the local instantaneous heat transfer coefficient $h(x, t)$ is first calculated from the simulation results using the following equation:

$$h(x, t) = \frac{q''}{(T_w(x, t) - T_{sat})} \quad (1)$$

where x represents the position along the central longitudinal axis of the conjugate heat transfer boundary, t represents the flow time, q'' is the applied heat flux in W/m^2 at the bottom surface of the solid domain, $T_w(x, t)$ is the temperature along the central longitudinal axis of the conjugate heat transfer boundary, for each of the saved time steps, and T_{sat} is the saturation temperature which is fixed. Then the average in time local heat transfer coefficient $\bar{h}(x)$ is calculated for each point along the sampling line, which is afterwards used for the calculation of the time averaged local $\overline{Nu}(x)$,

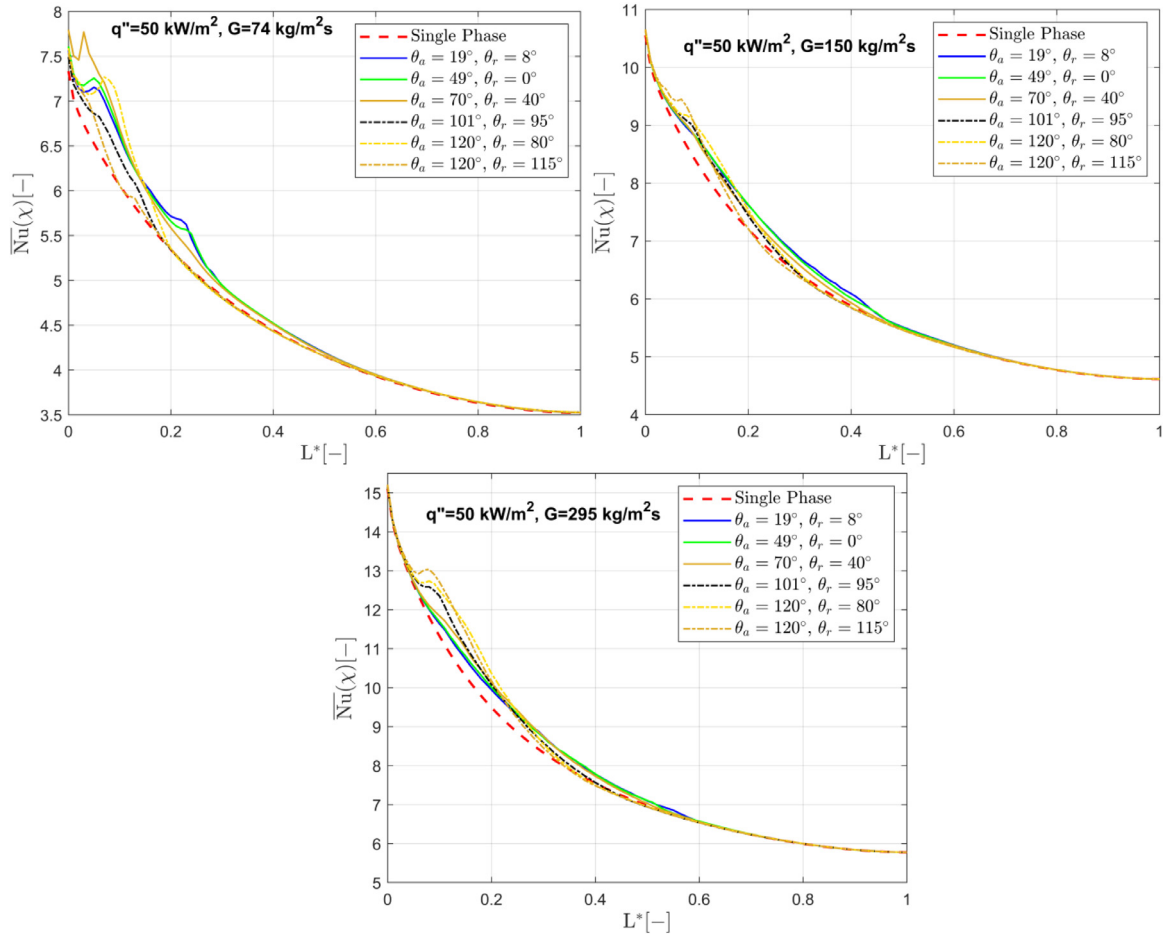


Fig. 10. Quantitative results of numerical cases examined for $q'' = 50 \text{ kW/m}^2$ and three different mass fluxes G (74, 150, 295 $\text{kg/m}^2\text{s}$). The global Nu number, which is defined as the area below the curves, is later compared to the area of the single-phase.

Table 5

Percentage difference between the global Nu number of the two-phase stage of each run with the corresponding single-phase for $q'' = 50 \text{ kW/m}^2$ and $G = 74, 150$ and $295 \text{ kg/m}^2\text{s}$.

$\theta_a / (^\circ)$	$\theta_r / (^\circ)$	$G / (\text{kg/m}^2\text{s})$	$Nu_{glob} / (-)$	% Diff.	$G / (\text{kg/m}^2\text{s})$	$Nu_{glob} / (-)$	% Diff.	$G / (\text{kg/m}^2\text{s})$	$Nu_{glob} / (-)$	% Diff.
Single-phase		74	4.493	-	150	6.012	-	295	7.809	-
19	8		4.634	3.13		6.153	2.35		7.966	2.01
49	0		4.638	3.22		6.145	2.21		7.974	2.10
70	40		4.644	3.37		6.103	1.15		7.989	2.30
101	95		4.538	1.00		6.077	1.07		7.975	2.12
120	80		4.593	2.24		6.105	1.54		8.028	2.80
120	115		4.519	0.57		6.063	0.84		8.007	2.53

Table 6

Percentage difference between the global Nu number and the single-phase for $q'' = 100 \text{ kW/m}^2$.

$\theta_a / (^\circ)$	$\theta_r / (^\circ)$	$G / (\text{kg/m}^2\text{s})$	$Nu_{glob} / (-)$	% Diff.	$G / (\text{kg/m}^2\text{s})$	$Nu_{glob} / (-)$	% Diff.	$G / (\text{kg/m}^2\text{s})$	Glob. Nu	% Diff.
Single-phase		74	4.493	-	150	6.0117	-	295	7.726	-
19	8		4.659	3.68		6.173	2.68		7.858	1.70
49	0		4.643	3.33		6.169	2.61		7.861	1.74
70	40		4.655	3.61		6.166	2.56		7.848	1.58
101	95		4.635	3.16		6.110	1.62		7.820	1.21
120	80		4.615	2.71		6.127	1.92		7.852	1.63
120	115		4.581	1.96		6.077	1.09		7.798	0.92

using the following equation:

$$\overline{Nu}(x) = \frac{\bar{h}(x)D_h}{\lambda_l} \quad (2)$$

where D_h is the hydraulic diameter of the channel and λ_l is the thermal conductivity of the liquid phase. Finally, the global aver-

aged Nusselt number (Nu_{glob}) is calculated as the area below the resulting in each case $\overline{Nu}(x)$ versus dimensionless length L^* curve using the following relationship through a Matlab script:

$$Nu_{glob} = \sum_{i=1}^n Nu_{j,n} / L^* \quad (3)$$

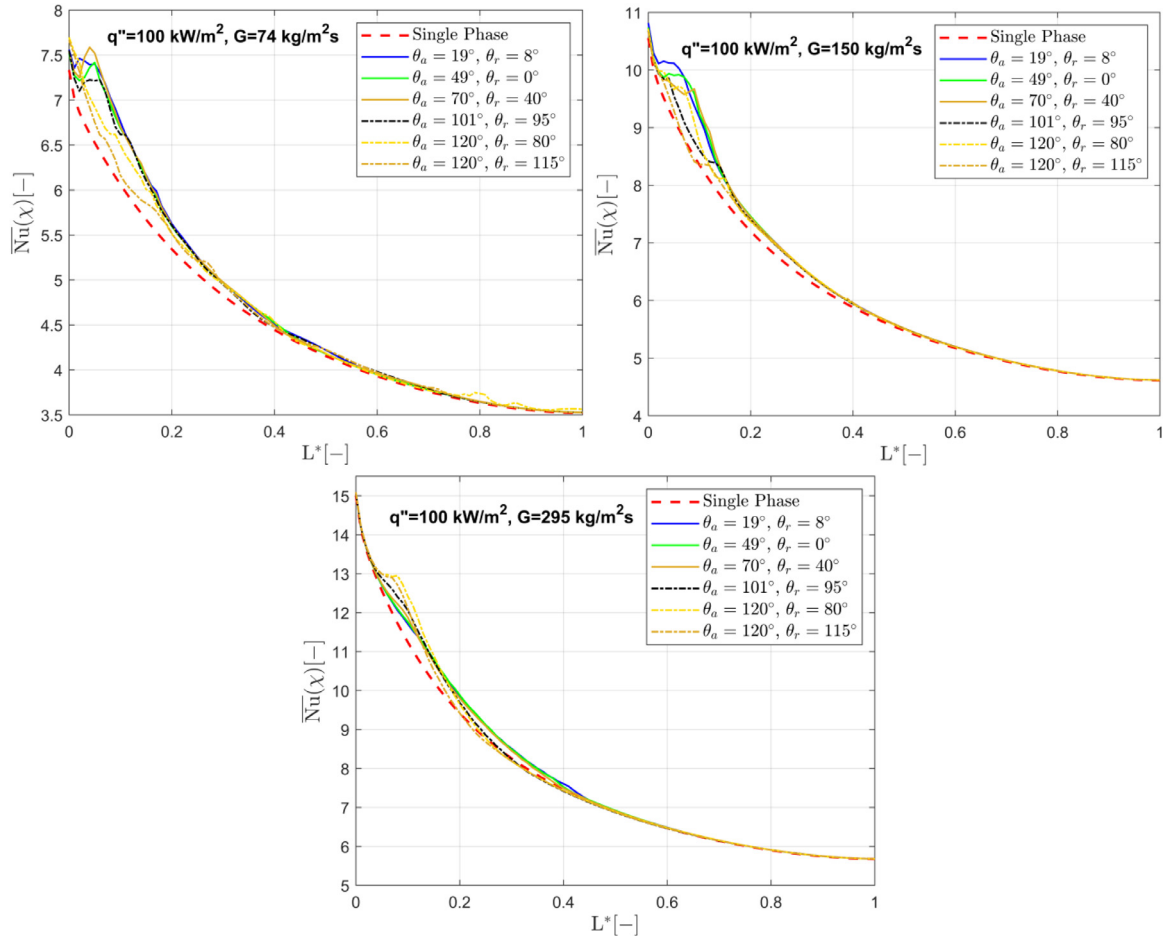


Fig. 11. Quantitative results of numerical cases examined for $q'' = 100 \text{ kW/m}^2$ and three different mass fluxes G (74, 150, 295 $\text{kg/m}^2\text{s}$). The global Nu number, which is defined as the area below the curves, is later compared to the area of the single-phase.

It is important to mention at this point that the single-phase stage of the numerical runs that is used as a reference for the local and/or global Nu numbers, might be much higher than the corresponding forced convection Nusselt numbers of a real single-phase flow, due to the fact that in the numerical simulation the nucleation is not a result of the simulation but instead a bubble is patched artificially in a previously developed single-phase flow that has reached a steady state without any nucleate boiling initiation when the onset temperature is reached. Therefore, this “numerical” single-phase stage is used here as a reference in order to identify and quantify the enhancement in the heat transfer from each two-phase flow stage that correspond to each combination of advancing and receding contact angles.

A quantitative comparison of the $\overline{Nu}(x)$ versus L^* , for $q'' = 20 \text{ kW/m}^2$ is conducted in Fig. 9, for $G = 74, 150, 295 \text{ kg/m}^2\text{s}$. For low mass flux, hydrophobic surfaces (solid line) appear to have slightly higher $\overline{Nu}(x)$ values compared to the hydrophilic surfaces (dash-dotted line). However, for medium and high mass fluxes the $\overline{Nu}(x)$ values in hydrophilic surfaces gradually decrease while in the hydrophobic surfaces gradually increase with respect to the single-phase flow reference curve.

The above observations are also reflected in Table 4, where the percentage difference of the Nu_{glob} between the single-phase reference and each two-phase flow result is depicted, for $q'' = 20 \text{ kW/m}^2$. It is evident that, hydrophilic surfaces perform better at $G = 74 \text{ kg/m}^2\text{s}$. This might be due to the fact that for cases with low and medium hydrophilicity, both liquid film

and contact line evaporation contribute in the overall heat transfer, while for the high hydrophilicity case heat transfer occurs only due to the contact line evaporation. For $G = 150 \text{ kg/m}^2\text{s}$, the differences between hydrophilic and hydrophobic cases can be considered as minor as the percentage difference with the single-phase flow reference is in all cases around 3%. Finally, hydrophilic surfaces and liquid film evaporation mechanism leads to inferior heat transfer performance, compared to the hydrophobic surface, at high mass flux $G = 295 \text{ kg/m}^2\text{s}$.

The time-averaged local Nu over the non-dimensional L^* (Nu_{glob}) of the considered hydrophilic and hydrophobic surfaces for the medium heat flux value $q'' = 50 \text{ kW/m}^2$ and all three investigated mass flux values is presented in Fig. 9.

Similar behavior is observed for the simulations of $q'' = 50 \text{ kW/m}^2$. As it can be seen from Fig. 10 and Table 5, for the mass fluxes of 74 and 150 $\text{kg/m}^2\text{s}$, for the hydrophilic surfaces where the liquid film evaporation has been the dominant heat transfer mechanism (for low mass flux: $\theta_a/\theta_r = 19^\circ/8^\circ$, $\theta_a/\theta_r = 49^\circ/0^\circ$, $\theta_a/\theta_r = 70^\circ/40^\circ$; and for medium mass flux: $\theta_a/\theta_r = 19^\circ/8^\circ$, $\theta_a/\theta_r = 49^\circ/0^\circ$), higher Nu_{glob} is observed. For mass flux 295 $\text{kg/m}^2\text{s}$, hydrophobic surfaces with the underpinned contact line evaporation mainly contributing towards the overall heat transfer, perform slightly better than the hydrophilic cases. Among the three hydrophobic cases, the surface with the high CAH hysteresis shows the highest increase in the overall heat transfer in comparison to the single-phase flow reference. The reason for this is expected to be the comparatively higher radius of the curvature of the nose which in some cases has resulted to the presence of

liquid film, and therefore, enhancement of heat transfer, due to a combination of liquid film and contact line evaporation.

Finally, the Nu_{glob} for the high heat flux value ($q'' = 100 \text{ kW/m}^2$), for all of the investigated advancing and receding contact angle combinations as well as the percentage difference between the Nu_{glob} of the two-phase flows and with the corresponding single-phase flow references, are summarised in Fig. 11 and Table 6, respectively. Overall, it can be seen that hydrophilic surfaces show slightly better performance for all mass fluxes compared to the hydrophobic. Additionally, it can be seen that the decrease of the mass flux results in a corresponding decrease of the percentage difference between the two-phase simulations and the corresponding single-phase flow reference. As mentioned earlier, churn flow was observed for the low mass flux simulations for all surfaces.

From all these quantitative comparison and analysis of the numerical simulation predictions, the following conclusions can be made:

- 1) Overall, as expected for the same heat flux, the Nu_{glob} is increased linearly with the corresponding increase of the mass flux.
- 2) In all graphs at $L^* = 0$, the curve starts with the maximum local time-averaged Nu number in the inlet region of the considered microchannel. This can be attributed due to the sudden release of the patched bubble.
- 3) In many cases up to $L^* = 0.15$, a sudden increase of the time-averaged Nu is observed. This behavior is related to the nucleation of the bubble and the rapid bubble growth in this region.
- 4) For $q'' = 20 \text{ kW/m}^2$ the Nu_{glob} curve of two-phase simulation cases and numerical single-phase diminish the difference and have almost same results after the $L^* = 0.7$. For higher mass fluxes the difference between the two-phase and single-phase is approximately at $L^* = 0.5$.
- 5) The local time-averaged Nu varies with respect to the existent flow boiling regime and the corresponding heat transfer mechanism, which were found to be: a) film boiling evaporation and b) contact line evaporation.
- 6) For the same heat flux applied, the hydrophilic surfaces result in better heat transfer performance for low mass flux ($G = 74 \text{ kg/m}^2\text{s}$). Hydrophilic surfaces perform slightly better for the medium mass flux cases ($G = 150 \text{ kg/m}^2\text{s}$) as well, with the only exemption of the case with low heat flux ($q'' = 20 \text{ kW/m}^2$), where the Nu_{glob} of hydrophobic cases is marginally higher, compared to the hydrophilic cases. For the highest mass flux value ($G = 295 \text{ kg/m}^2\text{s}$) and the lowest heat flux value ($q'' = 20 \text{ kW/m}^2$), hydrophobic cases performed better. Conversely, for $G = 295 \text{ kg/m}^2\text{s}$, the cases which have as dominant heat transfer mechanism the contact line evaporation it is shown to perform slightly worse, when the value of the heat flux increases (e.g. 50 and 100 kW/m^2).
- 7) When it comes to the Nu_{glob} and percentage difference with respect to the reference single-phase stages of the simulations, the highest difference between the hydrophilic and the hydrophobic surfaces is found to be between the two extreme contact angle cases ($\theta_a = 19^\circ$, $\theta_r = 8^\circ$ versus $\theta_a = 120^\circ$, $\theta_r = 115^\circ$) for $q'' = 20 \text{ kW/m}^2$ and $G = 295 \text{ kg/m}^2\text{s}$. Particularly, the hydrophobic surface had percentage difference of 4.79% compared to 2.39% of the hydrophilic case (approx. 2.4% difference). The smaller percentage difference is found to be for $q'' = 50 \text{ kW/m}^2$ and $G = 295 \text{ kg/m}^2\text{s}$ between $\theta_a = 19^\circ$, $\theta_r = 8^\circ$ and $\theta_a = 120^\circ$, $\theta_r = 80^\circ$, with the hydrophilic case to have percentage difference of 2.01% and the hydrophobic surface 2.80% (approx. 0.8% difference).

Overall, it can be concluded that for the examined heat and mass flux ranges, the effect of wettability plays a significant role

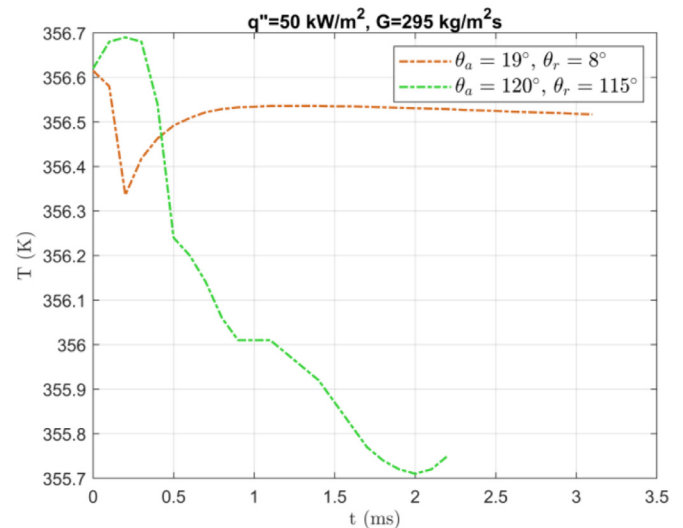


Fig. 12. Temperature at the point where the bubble seed is patched over time until the bubble reaches the outlet of the microchannel for $q'' = 50 \text{ kW/m}^2$ and $G = 295 \text{ kg/m}^2\text{s}$.

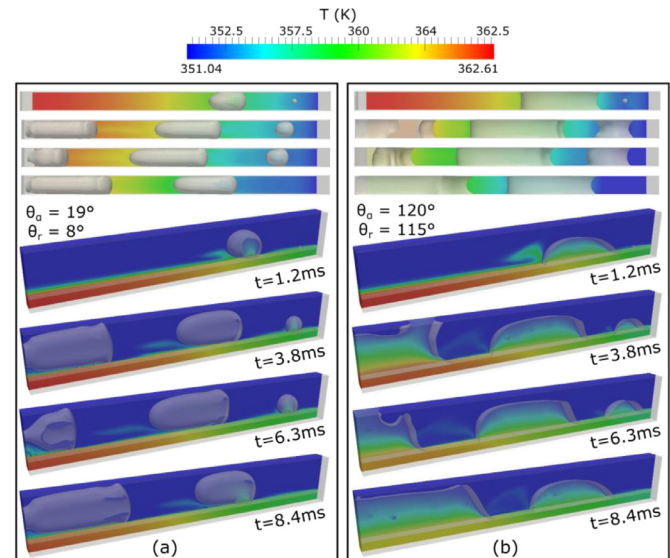


Fig. 13. Simulation results of a single bubble growth and multiple nucleation events with time interval 1.2 msec. The heat and mass flux values are 50 kW/m^2 and $295 \text{ kg/m}^2\text{s}$. (a) hydrophilic surface ($\theta_a/\theta_r = 19^\circ/8^\circ$), (b) hydrophobic surface ($\theta_a/\theta_r = 120^\circ/115^\circ$).

on the bubble growth dynamics that are directly linked to the developed flow regime causing a noticeable effect in the resulting heat transfer characteristics. However, considering a single nucleation site and a single nucleation event the effect of wettability on Nu_{glob} is evident but not significant.

4.2. Effect of wettability on micro-passages – Single nucleation site, multiple recurring nucleation events

In a wide range of practical applications, considering a single nucleation site, bubble nucleation constitutes a recurring event. Therefore, in order to create a more realistic case where the initiated nucleation event is recurring, an additional numerical study is performed using the same simulation setup but with multiple recurring single nucleation events for the same overall flow time interval. In total two simulations are conducted; one for hydrophilic ($\theta_a = 19^\circ$, $\theta_r = 8^\circ$) and one for hydrophobic ($\theta_a = 120^\circ$, $\theta_r = 115^\circ$)

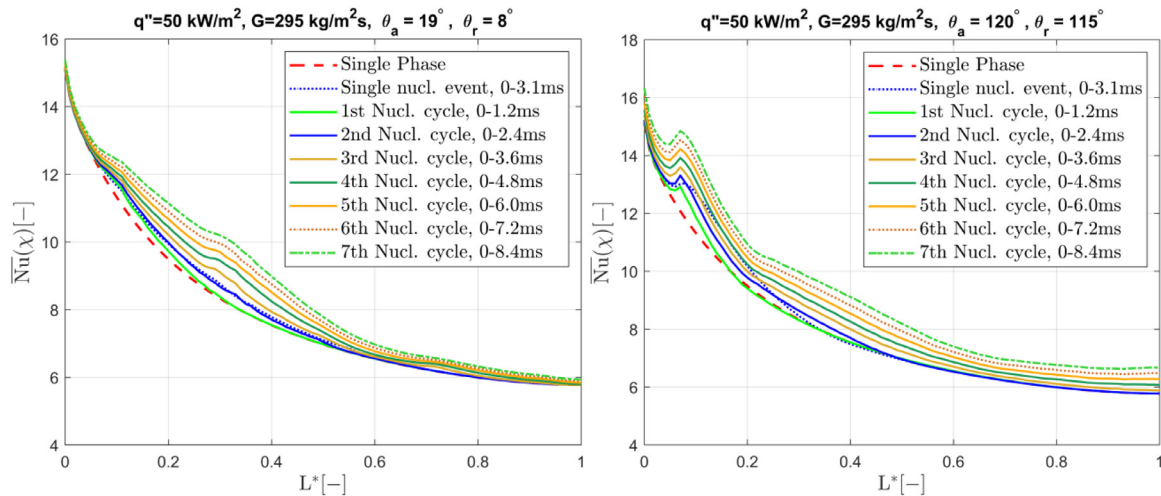


Fig. 14. Results of a single nucleation site and multiple nucleation events for $q'' = 50 \text{ kW/m}^2$ and $G = 295 \text{ Kg/m}^2\text{s}$. Comparison of the seven nucleation cycles with time interval 1.2ms with the single-phase reference simulation and the previous single nucleation event simulation. Left: Hydrophilic surface ($\theta_a/\theta_r = 19^\circ/8^\circ$). Right: Hydrophobic surface ($\theta_a/\theta_r = 120^\circ/115^\circ$).

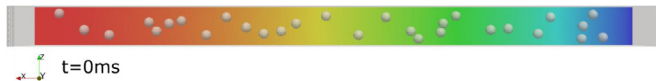


Fig. 15. Top view of the position of the 29 arbitrarily distributed along the heated microchannel bubble seeds. In total, seven recurring nucleation events of 29 nucleation sites, at the same position, were conducted.

surface. The applied heat and mass flux values are 50 kW/m^2 and $295 \text{ kg/m}^2\text{s}$, respectively. These values are specifically selected due to the fact that the Nu_{glob} percentage difference between the hydrophilic and hydrophobic surfaces, as can be seen in Table 5, are minimal, showing in this way the effect of wettability on multiple recurring nucleation events for the worst-case scenario heat and mass flux values.

In these simulations, after the initial patch of the bubble nucleus a new bubble is patched at the same point after a certain time period. The time interval that each bubble is patched is chosen to be 1.2ms. The first bubble is patched at 0ms, which corresponds to the time that the thermal boundary layer is fully developed (first single-phase stage of each simulation), up to 7.2ms, where the last bubble seed is patched. The simulations were run up to 8.4ms, completing seven nucleation cycles in total (one nucleation cycle = 1.2ms). All the bubble seeds were patched at the same position (same as in the previous simulations shown, at $200\mu\text{m}$ distance from the inlet of the microchannel). As it can be seen from Fig. 12, the proposed time interval has been selected after plotting the surface temperature (for a single nucleation event, shown in the previous section) at the nucleation point over time and it is found that this is the common point between the two surfaces for the temperature to stabilise for the first time, after its initial drop due the contact line evaporation. As mentioned earlier, the proposed numerical model does not include any prediction of the onset temperature. Therefore, in the following simulations, it is considered that the temperature at the surface is enough for producing multiple recurring nucleation events of a single bubble with the given frequency.

Qualitative, flow visualisation results of the multiple recurring nucleation events are shown in Fig. 13. In total, four different time periods using a 3D isometric view as well as a 2D top view of the investigated cases are depicted. The spatial and temporal evolution of the vapour bubble of the hydrophilic case is shown on the left side of the figure, while results for the same time pe-

riod of the hydrophobic surface can be seen on the right side. In both cases, a similar flow regime that resembles a slug flow can be observed, however, the dominant heat transfer mechanism is different in each case. In more detail, for the hydrophilic case, the imposed bubble seed maintains a contact area with the heated wall, at the early stages of each nucleation cycle. The average time needed for each bubble to completely detach from the heated wall is 1.5ms, after its appearance in the microchannel. Subsequently, the bubble(s) detaches from the surface covering almost the entire cross section of the channel, with the presence of a thin liquid film between the bubble and the channel walls. Some temporary dry patches with the side walls of the channel are evident at specific time periods. Therefore, in this case the dominant heat transfer mechanism is liquid film evaporation while contact line evaporation contributes only at the initial stages of the bubble growth after nucleation. On the contrary, the dominant heat transfer mechanism for the hydrophobic surface is in fact the contact line evaporation, with the growing bubble(s) maintaining contact area with the heated wall throughout the entire transport process. Moreover, it is characteristic that in the hydrophilic case, the bubbles are in continuous contact with the side walls of the channel throughout the entire process. In both surfaces, someone can clearly see that the colour of the surface near the outlet of the channel has changed from red (for $t=1.2\text{ms}$) into orange for the hydrophilic surface and into green for the hydrophobic surface (for $t=8.4\text{ms}$), reducing significantly the superheat of the wall, compared to the single nucleation event simulations. This is evident by seeing the quantitative results of the two simulations. In Fig. 14 the Nu_{glob} of each recurring nucleation cycle is compared with the reference single-phase curve as well as with the simulation presented in the previous section with the bubble growth from a single nucleation event for the same heat flux, mass flux and wettability.

In both figures it can be seen that each cycle is increasing the Nu_{glob} gradually, enhancing significantly the overall heat transfer. The percentage differences between the Nu_{glob} of each nucleation recurring event and the single-phase simulation, can be seen in Table 7. Initially it should be noted that the Nu_{glob} percentage difference of the hydrophilic surface (2.01%) was slightly lower than the hydrophobic surface (2.53%) for the single nucleation event simulations, and for every nucleation cycle this difference is farther increased. In more detail, the percentage difference of the Nu_{glob} for the hydrophilic surface from 0ms up to 8.4ms is 10.70%, while for the hydrophobic surface it is 16.31%. This difference for such

Table 7

Percentage difference between the global Nu number and the single-phase for $q'' = 50 \text{ kW/m}^2$ and $G = 295 \text{ kg/m}^2\text{s}$ for a hydrophilic and a hydrophobic surface.

$\theta_a, \theta_r / (^\circ)$	Bubble cycle	Bubble growth event duration / (ms)	% Difference
19, 8	Single nucl. event case	0-3.1	2.01
	1 st nucl. cycle	0-1.2	0.74
	2 nd nucl. cycle	0-2.4	1.95
	3 rd nucl. cycle	0-3.6	3.58
	4 th nucl. cycle	0-4.8	5.48
	5 th nucl. cycle	0-6.0	7.24
	6 th nucl. cycle	0-7.2	8.96
120, 115	Single nucl. event case	0-8.4	10.70
	1 st nucl. cycle	0-2.2	2.53
	2 nd nucl. cycle	0-1.2	0.57
	3 rd nucl. cycle	0-2.4	2.26
	4 th nucl. cycle	0-3.6	4.96
	5 th nucl. cycle	0-4.8	7.67
	6 th nucl. cycle	0-6.0	10.49
	7 th nucl. cycle	0-7.2	13.37
		0-8.4	16.31

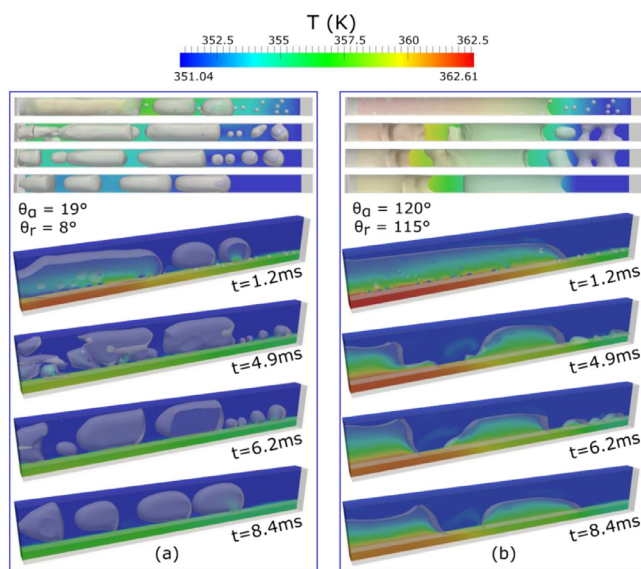


Fig. 16. Top and 3D views of the numerical results for $q'' = 50 \text{ kW/m}^2$ and $G = 295 \text{ kg/m}^2\text{s}$. (a) Single nucleation site and single nucleation event of bubble growth, for the last time period before the leading edge reaches the outlet of the channel, for a hydrophilic and hydrophobic surface. (b) Four different time periods for simulations of multiple nucleation sites (29 bubble seeds placed arbitrarily) and recurring nucleation cycles (1.2, 4.9, 6.2 and 8.4ms).

a small time frame and for the utilised mass flux, which was earlier shown that the wettability effect diminishes as the mass flux increases (for the $q'' = 50 \text{ kW/m}^2$), can be considered as a significant enhancement of the heat transfer due to the different surface wettability.

4.3. Effect of wettability on micro-passages – Multiple nucleation sites, multiple recurring nucleation events

In order to investigate an even more realistic case with respect to the previous investigations, numerical simulations of flow boiling in microchannels, with 29 recurring nucleation sites arbitrarily distributed on the heated wall, were also conducted. The simulations use the same parameters as the ones previously presented, where the heat and mass flux is 50 kW/m^2 and $295 \text{ kg/m}^2\text{s}$, respectively, and the bubble radius is $20 \mu\text{m}$. The 29 nucleation sites are recurring every 1.2ms, up to 8.4ms (seven nucleation cycles in total). The position of the 29 nucleation sites remains the same for

all recurring cycles. In Fig. 15, the position of the 29 arbitrarily distributed bubble seeds is shown at $t=0 \text{ ms}$.

Fig. 16 shows the evolution of phenomenon through four successive time instants. Again, as in the previous figures, a 2D top view and a 3D isometric view of the phenomenon for the hydrophilic and the hydrophobic surface can be seen. Qualitatively, it is evident that the flow regime can be affected from the total number of nucleation sites. Particularly, for the hydrophilic case, the transition from churn to slug flow is observed. Churn flow can be seen at the beginning of each cycle and mostly at the second half of the length of the microchannel, where the wall superheat is higher. This phenomenon is more profound in the early stages of the simulation and diminishes as the wall superheat decreases. Liquid film evaporation is the dominant heat transfer mechanism in the hydrophilic surface case, with small contribution of contact line evaporation, mostly in the first half of the microchannel, until the full departure of the bubbles from the heated surface. Conversely, slug flow is only observed for the hydrophobic surface and contact line evaporation is the only heat transfer mechanism.

By observing the colour of the heated wall at each time period for both surfaces, it is evident that the wall temperature of the hydrophilic surface due to the liquid film evaporation is considerably lower, resulting to a smaller wall superheat. Therefore, it seems that the liquid film evaporation is a more effective mechanism from the overall heat transfer. This can also be clearly seen from the local time-averaged Nu number for each nucleation cycle over the non-dimensional length L^* for the hydrophilic and hydrophobic surfaces shown in Fig. 17, as well as from Table 8, where the percentage difference between each nucleation cycle and the reference single-phase Nu_{glob} is shown.

As in the previous simulations of single nucleation bubble, the highest time-averaged Nu values are observed at the inlet of the channel. The hydrophobic surface performs better locally, and particularly within the first 15% of the microchannel length. After that, a sharp decrease of the time-averaged Nu up to 30% of the microchannels' length is observed, with the reduction continuing in a more moderate rate, up to the end of the channel. Even though the maximum local time-averaged Nu in the first 15% of the microchannel is lower in the hydrophilic surfaces, for the remainder 85% the time-averaged Nu is significantly higher.

Quantitatively, in both cases, it can be seen that the multiple nucleation events and the numerous nucleation events have significantly enhanced the heat transfer coefficient resulting in a higher Nu_{glob} . In the simulations of the single nucleation event and single nucleation site as well as in the case of single nucleation site with multiple recurring nucleation events, it has been concluded that

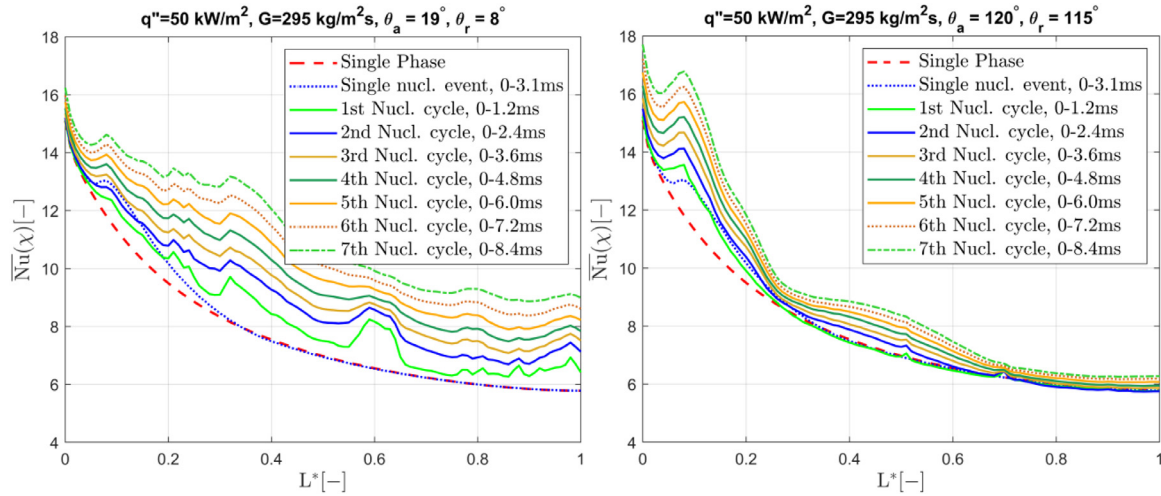


Fig. 17. Results of 29 nucleation bubble sites and multiple nucleation events for $q'' = 50 \text{ kW/m}^2$ and $G = 295 \text{ kg/m}^2\text{s}$. Comparison of the seven nucleation cycles with time interval 1.2ms with the single-phase simulation and the single nucleation event simulation, up to the point where the nose of the bubble touches the outlet of the microchannel. Left: Hydrophilic surface ($\theta_a/\theta_r = 19^\circ/8^\circ$). Right: Hydrophobic surface ($\theta_a/\theta_r = 120^\circ/115^\circ$).

Table 8

Percentage difference between the global Nu number and the single-phase for $q'' = 50 \text{ kW/m}^2$ and $G = 295 \text{ kg/m}^2\text{s}$ for a hydrophilic and a hydrophobic surface.

$\theta_a, \theta_r / (^\circ)$	Bubble cycle	Bubble growth event duration $t/(ms)$	% Difference
19, 8	Single nucl. event case	0-3.1	2.01
	1 st nucl. cycle	0-1.2	9.04
	2 nd nucl. cycle	0-2.4	16.21
	3 rd nucl. cycle	0-3.6	21.49
	4 th nucl. cycle	0-4.8	26.76
	5 th nucl. cycle	0-6.0	32.37
	6 th nucl. cycle	0-7.2	38.16
	7 th nucl. cycle	0-8.4	43.90
120, 115	Single nucl. event case	0-2.2	2.53
	1 st nucl. cycle	0-1.2	1.92
	2 nd nucl. cycle	0-2.4	4.76
	3 rd nucl. cycle	0-3.6	7.51
	4 th nucl. cycle	0-4.8	10.10
	5 th nucl. cycle	0-6.0	12.72
	6 th nucl. cycle	0-7.2	15.29
	7 th nucl. cycle	0-8.4	17.85

the hydrophobic surface performed slightly better compared to equivalent hydrophilic case. However, in this set of simulations, the hydrophobic surface performs better locally (from $L^*=0$ to 0.15), while the hydrophilic surface performs better overall, along the microchannel. The Nu_{glob} is increased in total by 43.9% compared to the single-phase. A very high Nu_{glob} enhancement of 17.8% compared to the single-phase can be seen also in the hydrophobic surface for all the nucleation cycles. The above findings agree well with previous studies that noted the remarkable effect of surface wettability on the flow boiling heat transfer, as presented in the introduction. Additionally, these verify the importance and the significance of the wettability on the global Nu number, and hence, on the time-averaged local Nu number.

5. Conclusions

CFD simulations have been performed for saturated flow boiling in a single rectangular channel having a hydraulic diameter of 200 μm and a channel length of 2.4mm in order to identify and quantify the effect of wettability characteristics on the resulting flow regimes as well as on the local and global heat transfer coefficients. The numerical experiments were conducted for six different surface wettabilities, with all the other parameters remaining the same. In total, three sets of simulations were performed:

- Simulations considering a single nucleation site and a single nucleation event, for heat fluxes of 20, 50 and 100 kW/m^2 and mass fluxes of 74, 150 and 295 $\text{kg/m}^2\text{s}$.
- Simulations considering single nucleation sites and seven recurring nucleation events every 1.2ms, for a heat flux 50 kW/m^2 and a mass flux 295 $\text{kg/m}^2\text{s}$.
- Multiple nucleation sites (29 bubble seeds arbitrarily distributed along the microchannel) and multiple (seven) nucleation recurring events every 1.2ms, for a heat flux 50 kW/m^2 and a mass flux 295 $\text{kg/m}^2\text{s}$.

The following remarks summarise the conclusions of the present investigation:

- Conclusions that are drawn from the simulations of a single nucleation site and a single nucleation event:
 - Surface wettability plays a significant role in the flow regime and the associated dominant heat transfer mechanism, for all the above described scenarios.
 - The effect of surface wettability on Nu_{glob} number for simulations with a single nucleation site and a single nucleation event is found to be minor.
 - Liquid film evaporation is the dominant heat transfer mechanism for hydrophilic surfaces.

- On hydrophobic surfaces contact line evaporation is found to be the main heat transfer mechanism.
 - By observing the local time-averaged $\overline{Nu}(x)$ over the non-dimensional length L^* plot, it can be seen that the hydrophobic surface performs better locally (e.g. from $L^*=0$ to 0.15), while the hydrophilic surface performs better in overall along the microchannel.
 - For a single nucleation event and a single nucleation site, hydrophilic surfaces performed better at low mass flux (74 kg/m²s), for all three examined heat fluxes, but also for the cases of high heat flux (100 kW/m²). Hydrophobic surfaces performed better for the cases with heat flux 20 kW/m² and mass flux 295 kg/m²s, and slightly better for heat flux 20 kW/m² and mass flux 150 kg/m²s as well as for 50 kW/m² and 295 kg/m²s. For the same set of simulations, when comparing the percentage difference between the Nu_{glob} of the numerical single-phase and each of the examined contact angle simulations, the highest difference between the hydrophilic and the hydrophobic surfaces is found to be between the two extreme contact angle cases ($\theta_a = 19^\circ$, $\theta_r = 8^\circ$ versus $\theta_a = 120^\circ$, $\theta_r = 115^\circ$) for $q'' = 20\text{ kW/m}^2$ and $G = 295\text{ kg/m}^2\text{s}$, where the hydrophobic surface had percentage difference of 4.79% compared to 2.39% of the hydrophilic case (approx. 2.4% difference). The smaller percentage difference is found to be for $q'' = 50\text{ kW/m}^2$ and $G = 295\text{ kg/m}^2\text{s}$ between $\theta_a = 19^\circ$, $\theta_r = 8^\circ$ and $\theta_a = 120^\circ$, $\theta_r = 80^\circ$, with the hydrophilic case to have percentage difference of 2.01% and the hydrophobic surface 2.80% (approx. 0.8% difference).
 - Among the hydrophilic surfaces, bubble departure from the heated surface is faster for the cases with low hydrophilicity (e.g. $\theta_a = 19^\circ$, $\theta_r = 8^\circ$ and $\theta_a = 49^\circ$, $\theta_r = 0^\circ$). For the case $\theta_a = 70^\circ$, $\theta_r = 40^\circ$ the high receding contact angle has led to either delayed bubble departure or no departure of the trailing part of the bubble, leading to two simultaneous heat transfer mechanisms (liquid film evaporation and contact line evaporation).
 - By increasing the applied heat flux value and keeping the mass flux constant, a minor effect on the time-averaged Nu number is observed, however, when the mass flux is increased, the heat transfer coefficient is found to increase linearly.
 - A slug flow regime is observed in all examined cases, except from the case with high heat flux and low mass flux (100 kW/m² and mass flux 295 kg/m²s), where churn flow can be seen at the initial stages of the nucleation. In both flow regimes, the bubbles grow within few milliseconds and fill almost the entire cross section of the microchannel.
- B) Conclusions that are drawn from the simulations of a single nucleation site and multiple recurring nucleation events:
- The flow regime did not change, remaining as a slug flow for both surfaces.
 - For the first two set of simulations, where numerical experiments of single nucleation site are conducted, contact line evaporation is found to be more efficient cooling mechanism, resulting in a higher heat transfer rate.
 - The Nu_{glob} is seen to be increased significantly, by each nucleation cycle, achieving within 8.4ms a 10.70% increase compared to the single-phase for the hydrophilic surface and 16.31% for the hydrophobic surface. Meaning that for the considered set of simulations as well as the heat and mass flux values, contact line evaporation, which is the dominant heat transfer mechanism for the hydrophobic surface, is more efficient.
- C) Conclusions that are drawn from the simulations of multiple nucleation sites and multiple nucleation recurring events:
- For the last set of simulations, where 29 arbitrarily distributed bubble seeds are patched and are periodically re-occurring for seven nucleation cycles, it is found that surface wettability plays a significant role on Nu_{glob} , and hence, on the heat transfer coefficient.
 - Within 8.4ms the Nu_{glob} is increased by 43.9%, compared to the single-phase. The increase of the hydrophobic surface compared to the single-phase is 17.8%.
 - For the hydrophobic case, a transition from churn flow to slug flow at the beginning of each nucleation cycle (e.g. within 0.2ms) can be observed at the second half of the length of the microchannel, where the wall superheat is higher. For the hydrophobic surface, only slug flow is observed.
 - Liquid film evaporation is the dominant heat transfer mechanism in the hydrophilic surface case, with small contribution of contact line evaporation, mostly in the first half of the microchannel until fully departure of the bubble from the heated surface occurs. On the other hand, contact line evaporation is the dominant heat transfer mechanism in the hydrophobic surface case.
 - The wettability effects on this set of simulations is expected to be even more effective on cases with low and/or high heat and mass flux (e.g. $q'' = 20\text{ kW/m}^2$ and $G = 295\text{ kg/m}^2\text{s}$), where the percentage difference for the first set of simulations was even higher, compared to heat and mass flux utilised in these cases.
 - By the presence of multiple nucleation sites, liquid film evaporation has significantly enhanced the overall heat transfer coefficient, and for the proposed simulation parameters it can be considered as a much more efficient heat transfer mechanism compared to contact line evaporation.
- Summarising, in the present paper for the first time in the literature, the effect of surface wettability in the bubble dynamics and the associated heat transfer characteristics, for cases of flow boiling within microchannels, is isolated, identified and quantified, giving significant insight into the wettability dependent dominance of the various different heat transfer mechanisms (liquid film versus contact line evaporation) providing their quantified effect, on the local and global heat transfer characteristics.

Declaration of Competing Interest

The authors declare that there is no conflict of interest.

CRediT authorship contribution statement

Konstantinos Vontas: Methodology, Software, Validation, Formal analysis, Investigation, Data curation, Writing - original draft, Writing - review & editing, Visualization. **Manolia Andredaki:** Software, Formal analysis, Writing - review & editing. **Anastasios Georgoulas:** Conceptualization, Software, Resources, Writing - review & editing, Validation, Funding acquisition, Project administration. **Nicolas Miché:** Writing - review & editing, Supervision, Funding acquisition. **Marco Marengo:** Conceptualization, Writing - review & editing, Supervision, Funding acquisition.

Acknowledgements

This research was partially funded through the European Union's Horizon 2020 research and innovation programme (Marie Skłodowska Curie grant agreement No. 801604), the European Space Agency (ESA MAP CORA projects TOPDESS and ENCOM4) and the UK's Engineering and Physical Science Research Council

(grant EP/P013112/1). Finally, Dr. Georgoulas would like to specifically thank also University of Brighton for the financial support through the Rising Stars Initiative 2019-2020 Scheme.

References

- [1] A. Wintrich, N. Ulrich, T. Werner, T. Reimann, Application Manual Power Semiconductors, 2015. <https://www.semikron.com/service-support/application-manual.html>.
- [2] T.G. Karayiannis, M.M. Mahmoud, Flow boiling in microchannels: Fundamentals and applications, *Appl. Therm. Eng.* 115 (2017) 1372–1397, doi:10.1016/j.applthermaleng.2016.08.063.
- [3] W.J. Minkowycz, E. Sparrow, J.P. Abraham, Nanoparticle Heat Transfer and Fluid Flow, 1st Edition, CRC Press, Boca Raton, 2013, doi:10.1201/b12983.
- [4] B. Yang, P. Wang, A. Bar-Cohen, Mini-contact enhanced thermoelectric cooling of hot spots in high power devices, *IEEE Trans. Components Packag. Technol.* 30 (2007) 432–438, doi:10.1109/TCAPT.2007.898744.
- [5] J. Kong, S.W. Chung, K. Skadron, Recent thermal management techniques for microprocessors, *ACM Comput. Surv.* 44 (2012), doi:10.1145/2187671.2187675.
- [6] I. Mudawar, Assessment of high-heat-flux thermal management schemes, *IEEE Trans. Components Packag. Technol.* 24 (2001) 122–141, doi:10.1109/6144.926375.
- [7] P. Cheng, H.Y. Wu, Mesoscale and Microscale Phase-Change Heat Transfer, *Adv. Heat Transf.* 39 (2006) 461–563, doi:10.1016/S0065-2717(06)39005-3.
- [8] A. Recinella, S.G. Kandlikar, Enhanced Flow Boiling Using Radial Open Microchannels With Manifold and Offset Strip Fins, *J. Heat Transfer*. 140 (2017) 21502–21509.
- [9] K.P. Drummond, D. Back, M.D. Sinanis, D.B. Janes, D. Peroulis, J.A. Weibel, S.V. Garimella, A hierarchical manifold microchannel heat sink array for high-heat-flux two-phase cooling of electronics, *Int. J. Heat Mass Transf.* 117 (2018) 319–330, doi:10.1016/j.ijheatmasstransfer.2017.10.015.
- [10] P. Cheng, G. Wang, X. Quan, Recent work on boiling and condensation in microchannels, *J. Heat Transfer*. 131 (2009) 1–15, doi:10.1115/1.3072906.
- [11] J.F. Tullius, R. Vajtai, Y. Bayazitoglu, A review of cooling in microchannels, *Heat Transf. Eng.* 32 (2011) 527–541, doi:10.1080/01457632.2010.506390.
- [12] B.J. Jones, S.V. Garimella, Surface roughness effects on flow boiling in microchannels, *J. Therm. Sci. Eng. Appl.* 1 (2009) 1–9, doi:10.1115/1.4001804.
- [13] M.M. Mahmoud, T.G. Karayiannis, D.B.R. Kenning, Surface effects in flow boiling of R134a in microtubes, *Int. J. Heat Mass Transf.* 54 (2011) 3334–3346, doi:10.1016/j.ijheatmasstransfer.2011.03.052.
- [14] K. Zhou, C. Coyle, J. Li, J. Buongiorno, W. Li, Flow boiling in vertical narrow microchannels of different surface wettability characteristics, *Int. J. Heat Mass Transf.* 109 (2017) 103–114, doi:10.1016/j.ijheatmasstransfer.2017.01.111.
- [15] A.M. Barajas, R.L. Pantón, The effects of contact angle on two-phase flow in capillary tubes, *Int. J. Multiph. Flow*. 19 (1993) 337–346, doi:10.1016/0301-9322(93)90007-H.
- [16] P. Rapolu, S.Y. Son, Characterization of wettability effects on pressure drop of two-phase flow in microchannel, *Exp. Fluids*. 51 (2011) 1101–1108, doi:10.1007/s00348-011-1129-8.
- [17] T. Cubaud, U. Ulmanella, C.M. Ho, Two-phase flow in microchannels with surface modifications, *Fluid Dyn. Res.* 38 (2006) 772–786, doi:10.1016/j.fluidyn.2005.12.004.
- [18] S.C. Cho, Y. Wang, Two-phase flow dynamics in a micro channel with heterogeneous surfaces, *Int. J. Heat Mass Transf.* 71 (2014) 349–360, doi:10.1016/j.ijheatmasstransfer.2013.12.023.
- [19] S.G. Kandlikar, Scale effects on flow boiling heat transfer in microchannels: A fundamental perspective, *Int. J. Therm. Sci.* 49 (2010) 1073–1085, doi:10.1016/j.jthermalsci.2009.12.016.
- [20] S.G. Kandlikar, W.J. Grande, Evolution of microchannel flow passages-thermohydraulic performance and fabrication technology, *Heat Transf. Eng.* 24 (2003) 3–17, doi:10.1080/01457630304040.
- [21] R. Rioboo, M. Marengo, S. Dall'Olio, M. Voue, J. De Coninck, An innovative method to control the incipient flow boiling through grafted surfaces with chemical patterns, *Langmuir* 25 (2009) 6005–6009, doi:10.1021/la900463b.
- [22] H. Wang, Y. Yang, M. He, H. Qiu, Subcooled flow boiling heat transfer in a microchannel with chemically patterned surfaces, *Int. J. Heat Mass Transf.* 140 (2019) 587–597, doi:10.1016/j.ijheatmasstransfer.2019.06.027.
- [23] J.M. Kim, T. Kim, D. In, H. Noh, M. Hwan, K. Moriyama, H. Sun, Effect of heterogeneous wetting surface characteristics on flow boiling performance, *Int. J. Heat Fluid Flow*. 70 (2018) 141–151, doi:10.1016/j.ijheatfluidflow.2018.02.006.
- [24] J. Kim, J.Y. Cho, J.S. Lee, Flow boiling enhancement by bubble mobility on heterogeneous wetting surface in microchannel, *Int. J. Heat Mass Transf.* 153 (2020) 1–13, doi:10.1016/j.ijheatmasstransfer.2020.119631.
- [25] H. Trieu Phan, N. Caney, P. Marty, S. Colasson, J. Gavillet, Flow Boiling of Water on Nanocoated Surfaces in a Microchannel, *J. Heat Transfer*. 134 (2011), doi:10.1115/1.4004935.
- [26] T.Y. Liu, P.L. Li, C.W. Liu, C. Gau, Boiling flow characteristics in microchannels with very hydrophobic surface to super-hydrophilic surface, *Int. J. Heat Mass Transf.* 54 (2011) 126–134, doi:10.1016/j.ijheatmasstransfer.2010.09.060.
- [27] W. Li, K. Zhou, J. Li, Z. Feng, H. Zhu, Effects of heat flux, mass flux and two-phase inlet quality on flow boiling in a vertical superhydrophilic microchannel, *Int. J. Heat Mass Transf.* 119 (2018) 601–613, doi:10.1016/j.ijheatmasstransfer.2017.11.145.
- [28] W. Li, Z. Chen, J. Li, K. Sheng, J. Zhu, Subcooled flow boiling on hydrophilic and super-hydrophilic surfaces in microchannel under different orientations, *Int. J. Heat Mass Transf.* 129 (2019) 635–649, doi:10.1016/j.ijheatmasstransfer.2018.10.003.
- [29] C. Choi, J.S. Shin, D.I. Yu, M.H. Kim, Flow boiling behaviors in hydrophilic and hydrophobic microchannels, *Exp. Therm. Fluid Sci.* 35 (2011) 816–824, doi:10.1016/j.expthermflusci.2010.07.003.
- [30] S. Gong, P. Cheng, Numerical investigation of saturated flow boiling in microchannels by the lattice boltzmann method, *Numer. Heat Transf. Part A Appl.* 65 (2014) 644–661, doi:10.1080/10407782.2013.836025.
- [31] S. Gong, P. Cheng, Numerical simulation of pool boiling heat transfer on smooth surfaces with mixed wettability by lattice Boltzmann method, *Int. J. Heat Mass Transf.* 80 (2015) 206–216, doi:10.1016/j.ijheatmasstransfer.2014.08.092.
- [32] S. Gong, P. Cheng, Lattice Boltzmann simulations for surface wettability effects in saturated pool boiling heat transfer, *Int. J. Heat Mass Transf.* 85 (2015) 635–646, doi:10.1016/j.ijheatmasstransfer.2015.02.008.
- [33] H.Y. Hsu, M.C. Lin, B. Popovic, C.R. Lin, N.A. Patankar, A numerical investigation of the effect of surface wettability on the boiling curve, *PLoS One* 12 (2017) e0187175, doi:10.1371/journal.pone.0187175.
- [34] J. Kim, J.S. Lee, Numerical study on the effects of inertia and wettability on subcooled flow boiling in microchannels, *Appl. Therm. Eng.* 152 (2019) 175–183, doi:10.1016/j.applthermaleng.2019.02.064.
- [35] S. Hardt, F. Wondra, Evaporation model for interfacial flows based on a continuum-field representation of the source terms, *J. Comput. Phys.* 227 (2008) 5871–5895, doi:10.1016/j.jcp.2008.02.020.
- [36] U.K. Alugoglu, S.K. Dubey, A. Javed, International Journal of Heat and Mass Transfer 3D Transient heat transfer analysis and flow visualization study in diverging microchannel for instability mitigated two-phase flow : A numerical study, *Int. J. Heat Mass Transf.* 160 (2020) 120212, doi:10.1016/j.ijheatmasstransfer.2020.120212.
- [37] S.S. Bertsch, E.A. Groll, S.V. Garimella, A composite heat transfer correlation for saturated flow boiling in small channels, *Int. J. Heat Mass Transf.* 52 (2009) 2110–2118, doi:10.1016/j.ijheatmasstransfer.2008.10.022.
- [38] F. Yang, W. Li, X. Dai, C. Li, Flow boiling heat transfer of HFE-7000 in nanowire-coated microchannels, *Appl. Therm. Eng.* 93 (2016) 260–268, doi:10.1016/j.applthermaleng.2015.09.097.
- [39] K. Vontas, M. Andredaki, A. Georgoulas, K.S. Nikas, M. Marengo, in: Numerical Investigation of Droplet Impact on Smooth Surfaces with Different Wettability Characteristics: Implementation of a dynamic contact angle treatment in OpenFOAM, *Proc. ILASS-Europe 2017. 28th Conf. Liq. At. Spray Syst., Valencia, Spain, 2017*, pp. 1–8, doi:10.4995/ILASS2017.2017.5020.
- [40] A. Georgoulas, M. Andredaki, M. Marengo, An enhanced VOF method coupled with heat transfer and phase change to characterise bubble detachment in saturated pool boiling, *Energies* 10 (2017), doi:10.3390/en10030272.
- [41] E. Teodori, P. Pontes, A. Moita, A. Georgoulas, M. Marengo, A. Moreira, Sensible heat transfer during droplet cooling: Experimental and numerical analysis, *Energies* 10 (2017), doi:10.3390/en10060790.
- [42] K. Vontas, C. Boscaroli, M. Andredaki, A. Georgoulas, C. Crua, J.H. Walther, M. Marengo, Droplet Impact on Suspended Metallic Meshes: Effects of Wettability, Reynolds and Weber Numbers, *Fluids* 5 (2020) 1–28, doi:10.3390/fluids5020081.
- [43] P. Pontes, R. Cautela, E. Teodori, A.S. Moita, A. Georgoulas, A.L.N.M. Moreira, Bubble Dynamics and Heat Transfer on Biphasic Surfaces: Experiments and Numerical Simulation, *J. Bionic Eng.* 17 (2020) 1–13, doi:10.1007/s42235-020-0064-x.
- [44] X.F. Peng, G.P. Peterson, B.X. Wang, Frictional flow characteristics of water flowing through rectangular microchannels, *Exp. Heat Transf.* 7 (1994) 249–264, doi:10.1080/08916159408946484.
- [45] F. Magaletti, A. Georgoulas, M. Marengo, Unraveling low nucleation temperatures in pool boiling through fluctuating hydrodynamics simulations, *Int. J. Multiph. Flow*. 130 (2020), doi:10.1016/j.ijmultiphaseflow.2020.103356.
- [46] E.W. Lemmon, M.L. Huber, M.O. McLinden, REFPROP V 7.0, NIST, 2002.
- [47] A. Faghri, Y. Zhang, *Transport Phenomena in Multiphase Systems* (2006).
- [48] M. Andredaki, A. Georgoulas, M. Marengo, Accelerating Taylor Bubbles within Circular Capillary Channels: Break-up Mechanisms and Regimes, *Int. J. Multiph. Flow*. (2020), doi:10.1016/j.ijmultiphaseflow.2020.103488.
- [49] K. Vontas, M. Andredaki, A. Georgoulas, N. Miché, M. Marengo, Wettability effect on flow boiling characteristics within micro-passages, *Proc. 5th World Congr. Momentum, Heat Mass Transf* (2020) 1–9 <https://doi.org/10.11159/icmfmh20.149>.